An inverse elliptic problem of medical optics with experimental data

Jianzhong Su[*], Michael V. Klibanov[†], Yueming Liu[*], Zhijin Lin[§]
Natee Pantong[†‡] and Hanli Liu[§]

Abstract

A numerical method for an inverse problem for an elliptic equation with the running source at multiple positions is presented. The so-called "approximate global convergence" property of this method is proved for the discrete case. The performance of the algorithm is verified on experimental data for Diffusion Optical Tomography. Direct applications are in near-infrared laser imaging technology for stroke detection in brains of small animals.

Keywords: Approximate Global Convergence Property; Inverse Problem; Diffusion Optical Tomography; Experimental Data
AMS Subject Classifications: 65B21; 65D10; 65F10

This preprint is available on-line at http://www.ma.utexas.edu/mp_arc.

1 Introduction

We consider a Coefficient Inverse Problem (CIP) for a partial differential equation (PDE) - the diffusion model with the unknown potential. The boundary data for this CIP, which model measurements, are originated by a point source running along a part of a straight line. This PDE governs light propagation in a diffusive medium, such as, e.g. biological tissue, smog, etc.. Thus, our CIP is one of problems of Diffusion Optical Tomography (DOT). We are interested in applications of DOT to the detection of stroke in small animals using measurements of near infrared light originated by lasers. Hence, the above point source is the light source in our case. The motivation of imaging of small animals comes from the idea that it might be a model case for the future stroke detection in humans via DOT. We

[*]Department of Mathematics, University of Texas at Arlington, Arlington, TX 76019, USA, su@uta.edu
[†]Department of Mathematics and Statistics, University of North Carolina at Charlotte, Charlotte, NC 28223, USA, mklibanv@uncc.edu
[‡]Department of Mathematics and Computer Science, Royal Thai Air Force Academy, Bangkok, Thailand
[§]Department of Bioengineering, University of Texas at Arlington, Arlington, TX 76019, USA

apply our numerical method to a set of experimental data for a phantom medium modeling the mouse's brain. Although this algorithm was developed in earlier publications [18,22-24] of this group, its experimental verification is new.

As to our numerical method, we introduce a new concept of the "approximate global convergence" property. In the previous publication [18] of this group about this method the approximate global convergence property was established in the continuos case. Compared with [18], the main new analytical result here is that we establish this property for the more realistic discrete case. In the convergence analysis of [18] the Schauder theorem [16] was applied for $C^{2+\alpha}-$solutions of certain elliptic equations arising in our method. Now, however, since we consider the discrete case, we use the Lax-Milgram theorem. Here and below $C^{m+\alpha}$ are Hölder spaces [16], where $m \geq 0$ is an integer and $\alpha \in (0,1)$.

CIPs are both nonlinear and ill-posed. These two factors cause very serious challenges in their numerical treatments. Indeed, corresponding least squares Tikhonov regularization functionals usually suffer from multiple local minima and ravines. As a result, conventional numerical methods for CIPs are locally convergent ones, see, e.g. [4,5] and references cited there. To have a guaranteed convergence to a true solution, a locally convergent algorithm should start from a point which is located in a small neighborhood of this solution. However, it is a rare case in applications when such a point is known. The main reason why our method avoids local minima is that it uses the structure of the underlying PDE operator and does not use a least squares functional.

By one of fundamental concepts of the theory of Ill-Posed Problems, one should assume the existence of an exact solution of such a problem for the case of an "ideal" noiseless data [25]. Although this solution is never known and is never achieved in practice (because of the noise in the real data), the regularization theory says that one needs to construct a good approximation for it [25]. We assume that a CIP has an exact solution for noiseless data and also assume that such a solution is unique.

It follows from the above discussion that it is important to develop such a numerical method which would have a rigorous guarantee of providing a point in a small neighborhood of that exact solution without any a priori knowledge of this neighborhood. Because of the above mentioned very serious difficulties of the goal of the development of such algorithms, it is unlikely that such a numerical method would not rely on some approximations. This is the reason why the notion of the approximate global convergence property was introduced in the recent work [20]. It is desirable to verify an approximately globally convergent numerical method on computationally simulated data, which was done in [18,22-24]. In this paper we make the next step: verify this method on experimental data. Regardless on some approximations we have here, the *main point* is that our numerical method does not rely on any a priori knowledge of a small neighborhood of the exact solution.

In [7-10,19,20] a similar numerical method for CIPs for a hyperbolic PDE was developed. The main difference of the technique of [7-10,19,20] with the current one is in the truncation of a certain integral. In [7-10,19,20] it was truncated at a high value $\overline{s} > 0$ of the parameter $s > 0$ of the Laplace transform of the solution of the underlying hyperbolic PDE. Indeed, in the hyperbolic case the truncated residual of that integral, which we call the "tail function",

is $O(1/\overline{s})$, as $\overline{s} \to \infty$, i.e. this residual is automatically small in this case. Being different from the hyperbolic case, in the elliptic PDE with the running source, $\overline{s} > 0$ represents the distance to the source. Because of this, the tail function is not automatically small in our case. Thus, a special effort to ensure this smallness was undertaken in [18], and this is repeated in the current publication. It was shown numerically in [18] that this special effort indeed improves the quality of the reconstruction, compare Figures 2b and 2c in [18].

Because of the above mentioned substantial challenges, the topic of the development of non-locally convergent numerical methods for CIPs is currently in its infancy. As to such methods for CIPs for elliptic PDEs, we refer to, e.g. publications [2,12,17,21] and references cited there. These publications are concerned with the Dirichlet-to-Neumann map (DN). We are not using the DN here.

The rest of this paper is arranged as follows. In section 2 we pose both forward and inverse problems and study some properties of the solution of the forward problem. In section 3 we present our numerical method. In section 4 we conduct the convergence analysis. In section 5 we discuss the numerical implementation of our method. In section 6 we describe the experiment. In section 7 we outline our procedure of processing of experimental data. In section 8 we present reconstruction results. We briefly summarize results in section 9.

2 Statement of the Problem

Our experimental data were collected at the boundary of a 2-D cross-section of the 3-D domain of interest. Hence, we have imaged this cross-section only and have ignored the dependence on the third variable. This is very similar with imaging from experimental data of [17], where images of a 2-D cross-section of a real human chest and heart beats were obtained using a non-local reconstruction algorithm of electrical impedance tomography. Because of this, we work here only with the 2-D mathematical model.

2.1 Mathematical definition of the Inverse Problem

Below $\mathbf{x} = (x, z) \in \mathbb{R}^2$ and $\Omega \subset \mathbb{R}^2$ is a convex bounded domain. The boundary of this domain $\partial\Omega \in C^3$ in our analysis. In numerical studies $\partial\Omega$ is piecewise smooth. Indeed, it is well known that there are always some discrepancies between the analysis and computational studies of numerical methods. Consider the following elliptic equation in $\mathbb{R}^2$ with the solution vanishing at infinity,

$$\Delta u - a(\mathbf{x})\, u = -\delta(\mathbf{x} - \mathbf{x}_0), \mathbf{x}, \mathbf{x}_0 \in \mathbb{R}^2, \tag{2.1}$$

$$\lim_{|\mathbf{x}| \to \infty} u(\mathbf{x}, \mathbf{x}_0) = 0. \tag{2.2}$$

Inverse Problem. *Let $k = const. > 0$. Suppose that in (2.1) the coefficient $a(\mathbf{x})$ satisfies the following conditions*

$$a \in C^1\left(\mathbb{R}^2\right),\ a(\mathbf{x}) \geq k^2 \text{ and } a(\mathbf{x}) = k^2 \text{ for } \mathbf{x} \in \mathbb{R}^2 \diagdown \Omega. \tag{2.3}$$

Let $L \subset \left(\mathbb{R}^2 \diagdown \overline{\Omega}\right)$ *be a straight line and* $\Gamma \subset L$ *be an unbounded and connected subset of* L. *Determine the function* $a(\mathbf{x})$ *inside of the domain* Ω, *assuming that the constant* k *is given and also that the following function* $\varphi(\mathbf{x}, \mathbf{x}_0)$ *is given*

$$u(\mathbf{x}, \mathbf{x}_0) = \varphi(\mathbf{x}, \mathbf{x}_0), \forall (\mathbf{x}, \mathbf{x}_0) \in \partial\Omega \times \Gamma. \tag{2.4}$$

We assume that sources $\{\mathbf{x}_0\}$ are located outside of the domain of interest Ω because this is the case of our measurements and because we do not want to work with singularities in our numerical method. As to the smoothness of the coefficient $a(\mathbf{x})$, we impose in (2.3) $a \in C^1(\mathbb{R}^2)$ rather than $a \in C^\alpha(\mathbb{R}^2)$ to shorten a certain part of the proof of Theorem 2.1.

Remark 2.1. The authors are unaware about a uniqueness theorem for this Inverse Problem. Nevertheless, because of applications, it makes sense to develop numerical methods for this problem, assuming that uniqueness holds. Therefore, following the above mentioned concept for ill-posed problems (section 1), we assume everywhere below that there exists the unique exact solution $a^*(\mathbf{x})$ of this problem for the "ideal" noiseless exact data $\varphi^*(\mathbf{x}, \mathbf{x}_0)$ in (2.4), and the function $a^*(\mathbf{x})$ satisfies conditions (2.3).

The CIP (2.1)-(2.4) has an application in imaging using light propagation in a diffuse medium, such as biological tissues. Since the modulated frequency equals zero in our case, then this is the so-called continuous-wave (CW) light. The coefficient $a(\mathbf{x}) = 3(\mu_s' \mu_a)(\mathbf{x})$, where $\mu_s'(\mathbf{x})$ is the reduced scattering coefficient and $\mu_a(\mathbf{x})$ is the absorption coefficient of the medium [3,4]. In the case of our particular interest in stroke detections in brains of small animals, the area of an early stroke can be modeled as a small sharp inclusion in an otherwise slowly fluctuating background. Usually the inclusion/ background contrast $a_{incl}/a_b \geq 2$. Therefore our focus is on the reconstruction of both locations of sharp small inclusions and the values of the coefficient $a(\mathbf{x})$ inside of them, rather than on the reconstruction of slow changing background functions.

2.2 Some Properties of the Solution of the Forward Problem (2.1), (2.2)

2.2.1 Existence and uniqueness

We now prove existence and uniqueness of the solution of the forward problem (2.1), (2.2). This result does not follow directly from classical results for elliptic PDEs [16], since they are formulated for bounded domains. For brevity we consider only the case $\mathbf{x}_0 \notin \overline{\Omega}$, since this is the case of our Inverse Problem. Let $K_p(z), z \in \mathbb{R}, p \geq 0$ be the Macdonald function. It is well known [1] that for $y \in \mathbb{R}$

$$K_p(y) = \frac{\sqrt{\pi}}{\sqrt{2y}} e^{-y} \left(1 + O\left(\frac{1}{y}\right)\right), y \to \infty. \tag{2.5}$$

Theorem 2.1. *Let* $\Omega \subset R^2$ *be a convex bounded domain with the boundary* $\partial\Omega \in C^3$. *Assume that the coefficient* $a(\mathbf{x})$ *satisfies conditions (2.3). Then for each source position*

$x_0 \in R^2 \setminus \overline{\Omega}$ there exists unique solution $u(\mathbf{x}, \mathbf{x}_0)$ of the problem (2.1), (2.2) such that

$$u(\mathbf{x}, \mathbf{x}_0) = \frac{1}{2\pi} K_0(k|\mathbf{x} - \mathbf{x}_0|) + \widehat{u}(\mathbf{x}, \mathbf{x}_0) := u_0(\mathbf{x} - \mathbf{x}_0) + \widehat{u}(\mathbf{x}, \mathbf{x}_0), \tag{2.6}$$

where the function u_0 is the fundamental solution of equation (2.1) with $a(\mathbf{x}) \equiv k^2$, the function $\widehat{u}$ satisfies (2.2), $\widehat{u} \in H^2(\mathbb{R}^2)$ and $\widehat{u} \in C^{2+\alpha}(\mathbb{R}^2)$. In addition, $u(\mathbf{x}, \mathbf{x}_0) > 0, \forall x \in \overline{\Omega}$.

Proof. We use the Laplace transform of fundamental solutions of some parabolic equations. Consider solutions of the following two parabolic Cauchy problems

$$v_t = \Delta v - \left(a(\mathbf{x}) - k^2\right) v, \ \ (\mathbf{x}, t) \in \mathbb{R}^2 \times (0, \infty), \tag{2.7}$$
$$v(\mathbf{x}, 0) = \delta(\mathbf{x} - \mathbf{x}_0); \tag{2.8}$$
$$v_{0t} = \Delta v_0, \ \ (\mathbf{x}, t) \in \mathbb{R}^2 \times (0, \infty), \tag{2.9}$$
$$v_0(\mathbf{x}, 0) = \delta(\mathbf{x} - \mathbf{x}_0). \tag{2.10}$$

It is well known that

$$v_0(\mathbf{x}, t) = \frac{1}{4\pi t} \exp\left(-\frac{|\mathbf{x} - \mathbf{x}_0|^2}{4t}\right). \tag{2.11}$$

Let $\mathbb{L}$ be the operator of the following version of the Laplace transform,

$$(\mathbb{L}f)(p) = \int_0^\infty f(t) \exp\left(-p^2 t\right) dt, p > 0, \tag{2.12}$$

for all appropriate functions f. Using (2.11), we obtain that the integral (2.12) for $f := v_0$ converges absolutely for all $p > 0$, as long as $\mathbf{x} \neq \mathbf{x}_0$. Next, formula (29) in section 4.5 of the table of the Laplace transform of the book [6] implies that for $p := k$

$$(\mathbb{L}v_0)(k) = \frac{1}{2\pi} K_0(k|\mathbf{x} - \mathbf{x}_0|) = u_0(\mathbf{x} - \mathbf{x}_0), \mathbf{x} \neq \mathbf{x}_0. \tag{2.13}$$

Consider now the function $\widetilde{v} = v_0 - v$. By (2.7)-(2.10)

$$\left(k^2 - a(\mathbf{x})\right) v = \Delta \widetilde{v} - \widetilde{v}_t, \ \ (\mathbf{x}, t) \in \mathbb{R}^2 \times (0, \infty), \tag{2.14}$$
$$\widetilde{v}(x, 0) = 0. \tag{2.15}$$

Theorem 11 of Chapter 2 of the book [15] ensures that the fundamental solution of a general parabolic equation with "good" coefficients is positive. Hence, $v(\mathbf{x}, t) > 0$ for $t > 0$. Further (2.3) implies that $(k^2 - a(\mathbf{x}))\, v \leq 0$. It follows from (2.14), (2.15) and Theorem 9 of Chapter 2 of [15] (about positive solutions of the Cauchy problem for parabolic PDEs) that $\widetilde{v} = v_0 - v \geq 0$. This implies that

$$v_0 \geq v > 0. \tag{2.16}$$

Thus, since the integral (2.12) converges absolutely for $f := v_0, p := k$, then it also converges absolutely for $f := v, p := k$.

If we formally apply the operator $\mathbb{L}$ at $p := k$ to equation (2.7) with the initial condition (2.8), then we obtain equation (2.1), although condition (2.2) would be still questionable. Let

$$(\mathbb{L}v)(k) := \overline{v}(\mathbf{x}, \mathbf{x}_0). \tag{2.17}$$

By (2.16) $\overline{v}(\mathbf{x}, \mathbf{x}_0) > 0$. Hence, it follows from the above that in order to show that the function $\overline{v}(\mathbf{x}, \mathbf{x}_0)$ satisfies condition (2.1), we need to show that the integral (2.12) converges absolutely for $p := k$ when the function f in (2.12) is replaced with either of derivatives v_t, v_{xx}, v_{zz}. In addition, we need to show that $\overline{v}$ satisfies (2.2). It follows from (2.3), (2.7) and (2.8) that

$$v(\mathbf{x}, t) = v_0(\mathbf{x}, \mathbf{x}_0, t) - \int_0^t \int_\Omega \frac{1}{4\pi(t-\tau)} \exp\left(-\frac{|\mathbf{x}-\boldsymbol{\xi}|^2}{4(t-\tau)}\right) \left(a(\boldsymbol{\xi}) - k^2\right) v(\boldsymbol{\xi}, \tau)\, d\boldsymbol{\xi} d\tau. \tag{2.18}$$

First, we estimate derivatives v_x, v_z. Since they are estimated similarly, consider v_x only. Let $|a| \leq M$ for a constant $M > 0$. By (2.18)

$$v_x(\mathbf{x}, t) = v_{0x}(\mathbf{x}, \mathbf{x}_0, t) + \int_0^t \int_\Omega \frac{(x-\xi_1)}{8\pi(t-\tau)^2} \exp\left(-\frac{|\mathbf{x}-\boldsymbol{\xi}|^2}{4(t-\tau)}\right) \left(a(\boldsymbol{\xi}) - k^2\right) v(\boldsymbol{\xi}, \tau)\, d\boldsymbol{\xi} d\tau. \tag{2.19}$$

Using (2.16) and (2.19), we obtain

$$|v_x| \leq |v_{0x}| + \left(M + k^2\right) \int_0^t \int_\Omega \frac{|\mathbf{x}-\boldsymbol{\xi}|}{8\pi(t-\tau)^2} \exp\left(-\frac{|\mathbf{x}-\boldsymbol{\xi}|^2}{4(t-\tau)}\right) v_0(\boldsymbol{\xi}, \tau)\, d\boldsymbol{\xi} d\tau. \tag{2.20}$$

Since $\mathbf{x}_0 \notin \overline{\Omega}$, then it follows from (2.11) that the function $v_0(\boldsymbol{\xi}, \tau)$ is bounded together with its derivatives for $(\boldsymbol{\xi}, \tau) \in \overline{\Omega} \times [0, \infty)$. The integral (2.20) has a weak singularity at the point $(\boldsymbol{\xi}, \tau) = (\mathbf{x}, t)$, which can be proven in a standard way (see, e.g. [15]): first, one needs to change variables in (2.20) to polar coordinates (r, φ), $r = |\mathbf{x} - \boldsymbol{\xi}|$. Next, one should change variables as $(r, \tau) \Leftrightarrow \left(z := r/\left(2\sqrt{t-\tau}\right), \tau\right)$. We obtain from formula (29) in section 4.5 of the table of the Laplace transform of the book [6] that

$$\mathbb{L}\left[\frac{|\mathbf{x}-\boldsymbol{\xi}|}{8\pi(t-\tau)^2} \exp\left(-\frac{|\mathbf{x}-\boldsymbol{\xi}|^2}{4(t-\tau)}\right)\right](k) = \frac{k}{2\pi} K_1(k|\mathbf{x}-\boldsymbol{\xi}|). \tag{2.21}$$

Hence, by (2.20), (2.21) and the convolution theorem

$$\int_0^\infty |v_x| e^{-k^2 t} dt \leq \frac{k}{2\pi} K_1(k|\mathbf{x}-\mathbf{x}_0|) + \frac{(Mk + k^3)}{2\pi} \int_\Omega K_1(k|\mathbf{x}-\boldsymbol{\xi}|) K_0(k|\boldsymbol{\xi}-\mathbf{x}_0|)\, d\boldsymbol{\xi}. \tag{2.22}$$

It is well known that for $y \to 0, y > 0$ the following asymptotic behavior takes place

$$K_1(y) = \frac{1}{y}(1 + O(y)), K_0(y) = -\ln y + \widehat{K}_0(y), \tag{2.23}$$

where the function $\widehat{K}_0(y)$ is bounded at $y \to 0, y > 0$. Hence, the integral in (2.22) has a weak singularity at the point $\{\boldsymbol{\xi} = \mathbf{x}\}$. Hence, using (2.5) and (2.17)-(2.23), we obtain $\overline{v}(\mathbf{x}, \mathbf{x}_0) \in L_2(\mathbb{R}^2)$, $[\overline{v}(\mathbf{x}, \mathbf{x}_0) - u_0(\mathbf{x} - \mathbf{x}_0)] \in C^1(\mathbb{R}^2)$ and functions $|\overline{v}|, |\overline{v}_x|, |\overline{v}_z|$ decay exponentially as $|\mathbf{x}| \to \infty$. Hence (2.2) is in place.

Consider now the second derivative v_{xx}. Using the integration by parts in (2.19), we obtain

$$v_x(\mathbf{x}, t) = v_{0x}(\mathbf{x}, \mathbf{x}_0, t) + \int_0^t \int_\Omega \frac{1}{4\pi(t-\tau)} \exp\left(-\frac{|\mathbf{x} - \boldsymbol{\xi}|^2}{4(t-\tau)}\right) \partial_{\xi_1}\left[\left(a(\boldsymbol{\xi}) - k^2\right) v(\boldsymbol{\xi}, \tau)\right] d\boldsymbol{\xi} d\tau.$$

Hence,

$$v_{xx}(\mathbf{x}, t) = v_{0xx}(\mathbf{x}, \mathbf{x}_0, t) + \int_0^t \int_\Omega \frac{(x - \xi_1)}{8\pi(t-\tau)^2} \exp\left(-\frac{|\mathbf{x} - \boldsymbol{\xi}|^2}{4(t-\tau)}\right) \partial_{\xi_1}\left[\left(a(\boldsymbol{\xi}) - k^2\right) v(\boldsymbol{\xi}, \tau)\right] d\boldsymbol{\xi} d\tau.$$

And similarly for v_{zz}, v_{xz}. Hence, similarly with the above we obtain that $[\overline{v}(\mathbf{x}, \mathbf{x}_0) - u_0(\mathbf{x} - \mathbf{x}_0)] \in C^2(\mathbb{R}^2)$ and functions $|\overline{v}_{xx}|, |\overline{v}_{xz}|, |\overline{v}_{zz}|$ decay exponentially as $|\mathbf{x}| \to \infty$. Next,

$$(\mathbb{L}v_t)(k) = \lim_{m \to \infty} \int_0^m v_t e^{-k^2 t} dt = \lim_{m \to \infty} v(\mathbf{x}, m) e^{-k^2 m} - \delta(\mathbf{x} - \mathbf{x}_0) + k^2 \lim_{m \to \infty} \int_0^m v e^{-k^2 t} dt.$$

It follows from (2.11) and (2.16) that the first limit here equals zero and the second limit is $(\mathbb{L}v)(k)$. Therefore, the function $\overline{v}(\mathbf{x}, \mathbf{x}_0)$ satisfies (2.1), (2.2).

Denote $\widehat{u}(\mathbf{x}, \mathbf{x}_0) = \overline{v}(\mathbf{x}, \mathbf{x}_0) - u_0(\mathbf{x} - \mathbf{x}_0)$. Then it from the above that $\widehat{u} \in H^2(\mathbb{R}^2) \cap C^2(\mathbb{R}^2), \forall \mathbf{x}_0 \notin \overline{\Omega}$. Furthermore, the function $\widehat{u}$ decays exponentially as $|\mathbf{x}| \to \infty$. Using (2.7)-(2.10), (2.13), we obtain

$$\Delta \widehat{u} - a(\mathbf{x}) \widehat{u} = \left(a(\mathbf{x}) - k^2\right) u_0, \mathbf{x} \in \mathbb{R}^2. \tag{2.24}$$

The right hand side of (2.24) does not have a singularity since $\mathbf{x}_0 \notin \overline{\Omega}$ and $a(\mathbf{x}) - k^2 = 0$ outside of the domain Ω. Hence, uniqueness of the problem (2.1), (2.2) for functions u represented by (2.6) with $\widehat{u} \in H^2(\mathbb{R}^2)$ can be easily obtained via a standard procedure: one should assume the existence of two solutions w_1, w_2, subtract equation (2.24) for w_2 from the same equation for w_1, multiply the resulting equation by $(w_1 - w_2)$ and integrate over $\mathbb{R}^2$ using integration by parts and the inequality $a(\mathbf{x}) \geq k^2$. Since the function $\widehat{u} \in C^2(\mathbb{R}^2)$, then Lemma 6.16 of Chapter 6 of the book [16] implies that $\widehat{u} \in C^{2+\alpha}(\mathbb{R}^2)$. The positivity of the function $u(\mathbf{x}, \mathbf{x}_0)$ follows from (2.16). $\square$

2.2.2 The asymptotic behavior at $|\mathbf{x}_0| \to \infty$

It follows from (2.5) and (2.6) that the asymptotic behavior of the function $u_0(\mathbf{x}-\mathbf{x}_0)$ is

$$\begin{aligned} u_0(\mathbf{x}-\mathbf{x}_0) &= w_0(|\mathbf{x}_0|)\left(1+O\left(\frac{1}{|\mathbf{x}_0|}\right)\right), |\mathbf{x}_0| \to \infty, \\ w_0(|\mathbf{x}_0|) &= \frac{e^{-k|\mathbf{x}_0|}}{2\sqrt{2\pi|\mathbf{x}_0|}}. \end{aligned}$$

Denote $b(\mathbf{x}) = a(\mathbf{x}) - k^2$. Then by (2.3) $b(\mathbf{x}) = 0$ for $\mathbf{x} \in \mathbb{R}^2 \setminus \Omega$. Let M_1 be a positive constant. Denote

$$B(M_1) = \left\{ b \in C^1\left(\mathbb{R}^2\right) : \|b\|_{C^1(\overline{\Omega})} \leq M_1, b(\mathbf{x}) \geq 0, b(\mathbf{x}) = 0 \text{ for } \mathbf{x} \in \mathbb{R}^2 \setminus \Omega \right\}.$$

Also, let the function $p_\infty(\mathbf{x})$ satisfies conditions

$$p_\infty(\mathbf{x}) \in C^{2+\alpha}(|\mathbf{x}| \leq R), \forall R > 0, p_\infty \in H^2\left(\mathbb{R}^2\right). \tag{2.25}$$

and be the solution of the following problem

$$\Delta p_\infty - k^2 p_\infty - b(\mathbf{x}) p_\infty = b(\mathbf{x}), \mathbf{x} \in \mathbb{R}^2, \tag{2.26}$$

$$\lim_{|x| \to \infty} p_\infty(\mathbf{x}) = 0. \tag{2.27}$$

The uniqueness and existence of the solution of the problem (2.25)-(2.27) can be proven very similarly with Theorem 2.1. The only difference is that one should replace $\delta(\mathbf{x}-\mathbf{x}_0)$ with $b(\mathbf{x})$ in initial conditions (2.8), (2.10).

Lemma 2.1. $1 + p_\infty > 0$.

Proof. Let $\widetilde{p} = 1 + p_\infty$. Then

$$\Delta \widetilde{p} - k^2 \widetilde{p} - b(\mathbf{x}) \widetilde{p} = -k^2, \quad \lim_{|\mathbf{x}| \to \infty} \widetilde{p}(\mathbf{x}) = 1. \tag{2.28}$$

Consider a sufficiently large number $R > 0$ such that $\widetilde{p}(\mathbf{x}) \geq 1/2$ for $\mathbf{x} \in \{|\mathbf{x}| \geq R\}$. Then the maximum principle applied to equation (2.28) for $\mathbf{x} \in \{|\mathbf{x}| < R\}$ shows that $\widetilde{p}(\mathbf{x}) > 0$ in $\{|\mathbf{x}| < R\}$. $\square$

Lemma 2.2 [18]. *Let the function $b \in B(M_1)$. Then there exists a constant $M_2(M_1, \Omega) > 0$ such that*

$$\|\ln u(\mathbf{x}, \mathbf{x}_0) - \ln w_0(|\mathbf{x}_0|) - \ln(1 + p_\infty(\mathbf{x}))\|_{C^2(\overline{\Omega})} \leq \frac{M_2(M_1, \Omega)}{|\mathbf{x}_0|},$$

$$\mathbf{x}_0 \in \{|\mathbf{x}_0| > 1\} \cap \left(\mathbb{R}^2 \setminus \overline{\Omega}\right), \mathbf{x} \in \overline{\Omega}.$$

3 The Numerical Method

Although this method was described in [18] in detail, we still need to briefly outline it in subsections 3.1, 3.2 in order to focus on those points to which we refer in our convergence analysis. The material of subsection 3.3 is new. Without any loss of the generality we can set $s := |\mathbf{x}_0|$, assuming that only the parameter s changes when the source $\mathbf{x}_0$ runs along $\Gamma \subset L$. Indeed, if necessary, we can put the origin on the straight line L. Denote $u(\mathbf{x}, s) := u(\mathbf{x}, \mathbf{x}_0), \mathbf{x} \in \Omega, \mathbf{x}_0 \in \Gamma$. Since $\Gamma \cap \overline{\Omega} = \varnothing$ and the point source $\mathbf{x}_0 \in \Gamma$, then $\mathbf{x}_0 \notin \overline{\Omega}$. Since by Theorem 2.1 $u(\mathbf{x}, s) > 0, \forall \mathbf{x} \in \overline{\Omega}$, we can consider the function $\widetilde{w}(\mathbf{x}, s) = \ln u(\mathbf{x}, s)$ for $\mathbf{x} \in \Omega$. We obtain from (2.1) and (2.4)

$$\Delta \widetilde{w} + |\nabla \widetilde{w}|^2 = a(\mathbf{x}) \text{ in } \Omega, \tag{3.1}$$

$$\widetilde{w}(\mathbf{x}, s) = \varphi_1(\mathbf{x}, s), \forall (\mathbf{x}, s) \in \partial\Omega \times [\underline{s}, \overline{s}], \tag{3.2}$$

where $\varphi_1 = \ln \varphi$ and $\underline{s}, \overline{s}$ are two positive numbers, which should be chosen in numerical experiments.

3.1 The integral differential equation

We now "eliminate" the coefficient $a(\mathbf{x})$ from equation (3.1) via the differentiation with respect to s. However, to make sure that the resulting the so-called "tail function" is small, we use the above mentioned (Introduction) special effort of the paper [18]. Namely, we divide (3.1) by $s^p, p > 0$. In principle, any number $p > 0$ can be used. But since in computations we took $p = 2$, both here and in [18], then we use below only $p = 2$, for the sake of definiteness. Denote $w(\mathbf{x}, s) = \widetilde{w}(\mathbf{x}, s)/s^2$. Next, let $q(\mathbf{x}, s) := \partial_s w(\mathbf{x}, s) = \partial_s \left(s^{-2} \ln u(\mathbf{x}, s)\right)$, for $s \in [\underline{s}, \overline{s}]$. Then

$$w(\mathbf{x}, s) = -\int_s^{\overline{s}} q(\mathbf{x}, \tau)\, d\tau + T(\mathbf{x}), \mathbf{x} \in \Omega, s \in [\underline{s}, \overline{s}], \tag{3.3}$$

where $T(\mathbf{x})$ is the so-called "tail function". The exact expression for this function is of course $T(\mathbf{x}) = w(\mathbf{x}, \overline{s})$. However, since the function $w(\mathbf{x}, \overline{s})$ is unknown, we will use an approximation for the tail function, see subsection 5.2 as well as [18]. By the Tikhonov concept for ill-posed problems [25], one should have some a priori information about the solution of an ill-posed problem. Thus, we can assume the knowledge of a constant $M_1 > 0$ such that the function $a(\mathbf{x}) - k^2 = b(\mathbf{x}) \in B(M_1)$. Hence, it follows from Lemma 2.2 that

$$\begin{aligned} T(\mathbf{x}, \overline{s}) &= \frac{\ln w_0(\overline{s})}{\overline{s}^2} + \frac{\ln(1 + p_\infty(\mathbf{x}))}{\overline{s}^2} + \frac{g(\mathbf{x}, \overline{s})}{\overline{s}^3},\ \mathbf{x} \in \Omega,\ \forall \overline{s} > 1, \\ \nabla T(\mathbf{x}, \overline{s}) &= \frac{\nabla p_\infty(\mathbf{x})}{\overline{s}^2 (1 + p_\infty(\mathbf{x}))} + \frac{1}{\overline{s}^3} \nabla g(\mathbf{x}, \overline{s}),\ \mathbf{x} \in \Omega,\ \forall \overline{s} > 1, \\ \|g(\mathbf{x}, \overline{s})\|_{C^1(\overline{\Omega})} &\leq M_2(M_1, \Omega),\ \forall \overline{s} > 1,\ \forall b \in B(M_1), \end{aligned} \tag{3.4}$$

where the number $M_2(M_1,\Omega)$ is independent on $\bar{s}$. Differentiating (3.1) with respect to s, we obtain the following nonlinear integral differential equation for the function q [18]

$$\Delta q - \frac{2}{s}\int\limits_s^{\bar{s}} \Delta q(\mathbf{x},\tau)\,d\tau - 2s^2\nabla q \int\limits_s^{\bar{s}} \nabla q(\mathbf{x},\tau)\,d\tau \tag{3.5}$$

$$+4s\left(-\int\limits_s^{\bar{s}} \nabla q(\mathbf{x},\tau)\,d\tau + \nabla T\right)^2 + 2s^2\nabla T\nabla q = -\frac{2}{s}\Delta T.$$

In addition, (3.2) implies that

$$q(\mathbf{x},s) = \psi(\mathbf{x},s),\ \forall(\mathbf{x},s)\in\partial\Omega\times[\underline{s},\bar{s}], \tag{3.6}$$

$$\psi(\mathbf{x},s) = \partial_s\left(s^{-2}\ln\varphi(\mathbf{x},s)\right). \tag{3.7}$$

If we approximate well both functions q and T together with their derivatives up to the second order, then we can also approximate well the target coefficient $a(\mathbf{x})$ via backwards calculations, see (3.16), (3.17). Therefore, the main questions now is: *How to approximate well both functions q and T using (3.3), (3.5), (3.6)?* The problem (3.5), (3.6) is nonlinear. In addition, both functions q and T are unknown here. The reason why we can approximate both functions q and T is that we treat them differently: while we approximate q using an "inner" process based on equation (3.5), we approximate T separately via an "outer process".

3.2 Layer stripping with respect to the source position

In this subsection we present a layer stripping procedure with respect to s for approximating the function q, assuming that the function T is known. We approximate the function $q(\mathbf{x},s)$ as a piecewise constant function with respect to the source position s. We assume that there exists a partition $\underline{s}=s_N<s_{N-1}<\ldots<s_1<s_0=\bar{s}, s_{i-1}-s_i=h$ of the interval $[\underline{s},\bar{s}]$ with a sufficiently small grid step size h such that

$$q(\mathbf{x},s) = q_n(\mathbf{x}) \text{ for } s\in[s_n,s_{n-1}), n\geq 1;\ q_0\equiv 0. \tag{3.8}$$

Hence,

$$\int\limits_s^{\bar{s}} q(\mathbf{x},s)\,ds = (s_{n-1}-s)\,q_n(\mathbf{x}) + h\sum_{j=0}^{n-1} q_j(\mathbf{x}).$$

Let $\psi_n(\mathbf{x})$ be the average of the function $\psi(\mathbf{x})$ over the interval (s_n,s_{n-1}). Then we approximate the boundary condition (3.6) as a piecewise constant function with respect to s,

$$q_n(\mathbf{x}) = \psi_n(\mathbf{x}), \mathbf{x}\in\partial\Omega. \tag{3.9}$$

Using (3.8), integrate equation (3.5) with respect to $s \in [s_n, s_{n-1})$. We obtain for $n \geq 1$

$$\begin{gathered} \Delta q_n + A_{2,n}\left(h\sum_{j=0}^{n-1}\nabla q_j - \nabla T\right)\nabla q_n = \\ A_{1,n}\left(\nabla q_n\right)^2 + A_{3,n}h\sum_{j=1}^{n-1}\Delta q_j + A_{4,n}\left(h\sum_{j=0}^{n-1}\nabla q_j - \nabla T\right)^2 - A_{3,n}\Delta T, \end{gathered} \tag{3.10}$$

where $A_{k,n}, k = 1, ..., 4$ are certain numbers, see [18] for exact formulas for them. Assume that

$$\overline{s} > 1,\ h \in (0,1) \text{ and } \frac{h}{\overline{s}} < \frac{1}{2}. \tag{3.11}$$

Given (3.11), the following estimates hold [18]

$$|A_{1,n}| \leq 2\overline{s}^2 h, \tag{3.12}$$

$$\max_{i=2,3,4}\left(|A_{i,n}|\right) \leq 8\overline{s}^2 \text{ for } \overline{s} > 1. \tag{3.13}$$

The estimate (3.12) tells one that the nonlinearity $A_{1,n}\left(\nabla q_n\right)^2$ in equation (3.10) can be mitigated via decreasing the grid step size h. Thus, we assume below that h is so small that the number $2\overline{s}^2 h$ is negligible. Hence, we *approximately* set

$$A_{1,n}\left(\nabla q_n\right)^2 := 0. \tag{3.14}$$

In fact, our previous numerical experience of [18,23] tells us that the term $A_{1,n}\left(\nabla q_n\right)^2$ provides a very small influence on reconstruction results. The approximation (3.14) enables us to solve only linear elliptic Dirichlet boundary value problem (3.9), (3.10) for each q_n. We point out that, assuming (3.14), we do not linearize the original problem. Indeed, the nonlinearity is manifested in products $\nabla q_j \nabla p_n$ in (3.21). Denote

$$\overline{q}\left(\mathbf{x}\right) = \left(q_0, q_1, ..., q_N\right)\left(\mathbf{x}\right). \tag{3.15}$$

As soon as the vector function $\overline{q}\left(\mathbf{x}\right)$ is computed, we reconstruct approximations for functions $\widetilde{w}\left(\mathbf{x}, s_N\right), a\left(\mathbf{x}\right)$ via (see (3.1), (3.3) and (3.8))

$$\widetilde{w}\left(\mathbf{x}, s_N\right) = -s_N^2 h\sum_{j=0}^{N} q_j\left(\mathbf{x}\right) + s_N^2 T\left(\mathbf{x}\right), \tag{3.16}$$

$$a\left(\mathbf{x}\right) = \Delta\widetilde{w}\left(\mathbf{x}, s_N\right) + \left|\nabla\widetilde{w}\left(\mathbf{x}, s_N\right)\right|^2. \tag{3.17}$$

3.3 Weak formulation of the Dirichlet boundary value problem (3.9), (3.10) with the assumption (3.14)

We now formulate the Dirichlet boundary value problem (3.9), (3.10) with the approximation (3.14) in the weak form. We need this formulation for our convergence analysis in section 4. Assume that there exists functions Ψ_n such that

$$\Psi_n \in H^2\left(\Omega\right) \text{ and } \Psi_n|_{\partial\Omega} = \psi_n\left(\mathbf{x}\right), n \in [1, N]. \tag{3.18}$$

Denote $H_0^1(\Omega) = \{u \in H^1(\Omega) : u \mid_{\partial\Omega} = 0\}$. There exists a constant $C_1 = C_1(\Omega) = const. \geq 1$ such that

$$\|u\|_{L_2(\Omega)} \leq C_1 \|\nabla u\|_{H^1(\Omega)}, \ \forall u \in H_0^1(\Omega). \tag{3.19}$$

Assuming that (3.14) is valid, denote f_n the last 2 terms on the right hand side of the resulting equation (3.10),

$$f_n(\mathbf{x}) = A_{4,n}\left(h\sum_{j=0}^{n-1}\nabla q_j - \nabla T\right)^2 - A_{3,n}\Delta T. \tag{3.20}$$

Consider the function $p_n = q_n - \Psi_n$. Then (3.9), (3.10), (3.14) and (3.18) imply that

$$\Delta p_n + A_{2,n}\left(h\sum_{j=0}^{n-1}\nabla q_j - \nabla T\right)\nabla p_n =$$

$$-\left[\Delta\Psi_n + A_{2,n}\left(h\sum_{j=0}^{n-1}\nabla q_j - \nabla T\right)\nabla\Psi_n\right] + A_{3,n}h\sum_{j=0}^{n-1}\Delta q_j + f_n, \tag{3.21}$$

$$p_n \mid_{\partial\Omega} = 0.$$

Multiply both sides of equation (3.21) by an arbitrary function $\eta \in H_0^1(\Omega)$ and integrate over Ω using integration by parts. We obtain

$$\int_\Omega \nabla p_n \nabla\eta d\mathbf{x} - A_{2,n}\int_\Omega\left(h\sum_{j=0}^{n-1}\nabla q_j - \nabla T\right)\nabla p_n \cdot \eta d\mathbf{x}$$

$$= -\int_\Omega\left\{\nabla\Psi_n\nabla\eta + \left[A_{2,n}\left(h\sum_{j=0}^{n-1}\nabla q_j - \nabla T\right)\nabla\Psi_n + f_n\right]\eta\right\}d\mathbf{x} \tag{3.22}$$

$$+A_{3,n}\int_\Omega h\sum_{j=0}^{n-1}\nabla q_j\nabla\eta d\mathbf{x}, \ \forall\eta \in H_0^1(\Omega).$$

Hence, the function $q_n \in H^1(\Omega)$ is a weak solution of the problem (3.9), (3.10) with the approximation (3.14) if and only if the function $p_n = (q_n - \Psi_n) \in H_0^1(\Omega)$ satisfies the integral identity (3.22). The question about existence and uniqueness of the weak solution of the problem (3.22) is addressed in Theorem 4.1. This question is addressed only within the framework of our convergence analysis, since this is sufficient for our goal.

Assuming that conditions (3.18) hold for $n = 1, \ldots, N$, we now describe our algorithm of sequential solutions of boundary value problems (3.9), (3.10) with the approximation (3.14) for $n = 1, \ldots, N$, assuming that an approximation $T(\mathbf{x})$ for the tail function is found (see subsection 5.2 for the latter). Recall that $q_0 = 0$. Hence, we have:

Step $n \in [1, N]$. Suppose that functions $q_1, \ldots, q_{n-1}$ are computed. On this step we find the weak solution of the Dirichlet boundary problem (3.9), (3.10) with the approximation (3.14) for the function q_n via the FEM with triangular finite elements.

Step $N+1$. After functions $q_1, \ldots, q_N$ are computed, the function $a(\mathbf{x})$ is reconstructed using a certain analog of (3.16), (3.17) at $n := N$, i.e., for the lowest value of $s := s_N = \underline{s}$ as described in subsection 5.1.

Remark 3.1. If working only with weak solutions of the problem (3.22), we would not be able to estimate products $\nabla q_j \nabla p_n$, which are present in (3.22) due to the nonlinearity of the original equation (3.5). This is the reason why we need to assume that each function p_n is a linear combination of a finite number m of finite elements and the number m should have an upper bound, see (4.16). Indeed, all norms in a finite dimensional space are equivalent. There is nothing unusual that the number of finite elements should not be too large. Indeed, this number is quite often serves as a regularization parameter in ill-posed problems, see, e.g. [20] for a similar conclusion.

4 Convergence Analysis

By Remark 2.1 we should assume the existence and uniqueness of an "ideal" exact solution $a^*(\mathbf{x})$ of our inverse problem for an "ideal" noiseless exact data $\varphi^*(\mathbf{x}, \mathbf{x}_0)$ in (2.4). Next, in accordance with the regularization theory, one should assume the presence of an error in the data of the level ζ and construct an approximate solution for this case. Here $\zeta > 0$ is a small parameter.

4.1 Approximate global convergence

Definition 4.1 (approximate global convergence) [20]. Consider a nonlinear ill-posed problem. Suppose that a certain approximate mathematical model $\overline{M}$ is proposed to solve this problem numerically. Assume that, within the framework of the model $\overline{M}$, this problem has unique exact solution $x^* \in B$ for the noiseless data y^*. Here B is an appropriate Banach space with the norm $\|\cdot\|_B$. Consider an iterative numerical method for solving that problem. Suppose that this method produces a sequence of points $\{x_n\}_{n=1}^K \subset B, K \in [1, \infty)$. Let the number $\theta \in (0,1)$. We call this numerical method *approximately globally convergent of the level* θ *in the norm of the space* B, or shortly *globally convergent*, if, within the framework of the model $\overline{M}$, a theorem is proven, which claims that, without any knowledge of a sufficiently small neighborhood of x^*, there exists a number $\overline{K} \in [1, K)$ such that the following inequality is valid

$$\frac{\|x_n - x^*\|_B}{\|x_n\|_B} \leq \theta, \forall n \geq \overline{K}. \tag{4.1}$$

Suppose that iterations are stopped at a certain number $k \geq \overline{K}$. Then the point x_k is denoted $x_k := x_{glob}$ and is called *the approximate solution resulting from this method.*

Since Definition 4.1 represents a new concept, it is worthwhile to have some discussion of it. We present this discussion in this subsection. A similar discussion can be found in [20].

First, since the approximate mathematical model $\overline{M}$ is involved in Definition 4.1, then it is reasonable to somehow verify this model. This verification can be done via computational testing for simulated data, which was actually done in [18,22-24], although without Definition 4.1. In addition, it is also desirable to verify the model $\overline{M}$ on experimental data, which is done here.

Second, the main reason for Definition 4.1 is a substantial challenge in the goal of constructing such numerical method for a CIP, which would provide a good approximation for the exact solution without an advanced knowledge of a small neighborhood of this solution (section 1). It is precisely because of this challenge that we use the approximate mathematical model $\overline{M}$. Indeed, it is highly unlikely that the goal of constructing such algorithms would be achieved without some approximations. It is important that as soon as the model $\overline{M}$ is constructed, one should rigorously guarantee the achievement of that good approximation within the framework of this model.

Third, unlike the classical convergence, this definition does not require that $\lim_{n\to\infty} x_n = x^*$. Furthermore, the total number K of iterations can be finite. We refer to page 157 of the book [14] where it is stated that the number of iterations can be regarded as a regularization parameter sometimes for an ill-posed problem. This lesser requirement is only due to the difficulty in rigorous analysis only. In our computations both for simulated and experimental data, classical convergence in the Cauchy sense was achieved.

4.2 Exact solution

Since the exact solution was defined in [18], we outline it only briefly here for the convenience of the reader. The second reason of presenting this description here is that we need to refer to certain formulas of this subsection in our convergence analysis. Let the function $a^*(\mathbf{x})$ satisfying conditions (2.3) be the exact solution of our inverse problem for the noiseless data $\varphi^*(\mathbf{x}, \mathbf{x}_0)$ in (2.4). We assume that $a^*(\mathbf{x})$ is unique (Remark 2.1). We now need to introduce functions q_n^*, which are analogs of functions q_n for the case $a := a^*$. Let the function $u^*(\mathbf{x}, s)$ be the same as the function $u(\mathbf{x}, \mathbf{x}_0)$ in Theorem 2.1, but for the case $a(\mathbf{x}) := a^*(\mathbf{x})$. Denote

$$\begin{aligned} w^*(\mathbf{x}, s) &= s^{-2} \ln u^*(\mathbf{x}, s), \ q^*(\mathbf{x}, s) = \partial_s w^*(\mathbf{x}, s), \\ T^*(\mathbf{x}) &= w^*(\mathbf{x}, \overline{s}). \end{aligned}$$

The function q^* satisfies the following analogue of equation (3.5) with the boundary condition (3.6)

$$\begin{aligned} &\Delta q^* - \tfrac{2}{s}\int\limits_s^{\overline{s}} \Delta q^*(\mathbf{x}, \tau)\, d\tau - 2s^2 \nabla q^* \int\limits_s^{\overline{s}} \nabla q^*(\mathbf{x}, \tau)\, d\tau \\ &+4s\left(-\int\limits_s^{\overline{s}} \nabla q^*(\mathbf{x}, \tau)\, d\tau + \nabla T^*\right)^2 + 2s^2 \nabla q^* \nabla T^* = -\tfrac{2}{s}\Delta T^*, \ \mathbf{x} \in \Omega, \\ &q^*(\mathbf{x}, s) = \psi^*(\mathbf{x}, s), \forall (\mathbf{x}, s) \in \partial\Omega \times [\underline{s}, \overline{s}], \end{aligned} \tag{4.2}$$

where by (3.7) $\psi^*(\mathbf{x},s)=\partial_s\left(s^{-2}\ln u^*(\mathbf{x},s)\right)$ for $(\mathbf{x},s)\in\partial\Omega\times[\underline{s},\bar{s}]$. We call the function $q^*(\mathbf{x},s)$ *the exact solution* of the equation (4.2) with the exact boundary condition $\psi^*(x,s)$. By Theorem 2.1

$$q^*(\mathbf{x},s)\in C^{2+\alpha}\left(\overline{\Omega}\right)\times C^1[\underline{s},\bar{s}], \tag{4.3}$$

where C^1 dependent on $s\in[\underline{s},\bar{s}]$ is required specifically for our method of running source position. Although Theorem 2.1 does not claim the $C^{2+\alpha}\left(\overline{\Omega}\right)-$ smoothness of the derivative $\partial_s u^*(\mathbf{x},s)$, actually this smoothness can be derived from (2.6). We do not present this derivation for brevity.

By one of fundamental concepts of the theory of Ill-Posed Problems mentioned in subsection 3.1, we can impose some a priori bounds in the solution, we assume the knowledge of an upper bound for the function q^*. Thus we assume that we know a constant C^* such that

$$\begin{aligned}\|q^*\|_{C^{2+\alpha}\left(\overline{\Omega}\right)\times C^1[\underline{s},\bar{s}]} &\leq C^*, &(4.4)\\ C^* &= const.\geq 1. &(4.5)\end{aligned}$$

Let $q_n^*(\mathbf{x})$ and $\psi_n^*(\mathbf{x})$ be averages over the interval (s_n,s_{n-1}) of functions $q^*(\mathbf{x},s)$ and $\psi^*(\mathbf{x},s)$ respectively. Then by (4.3)-(4.5) it is reasonable to assume that

$$\max_{n\in[1,n]}\max_{s\in[s_n,s_{n-1}]}\left(\|q^*(\mathbf{x},s)-q_n^*(\mathbf{x})\|_{C^{2+\alpha}\left(\overline{\Omega}\right)}+\|\psi^*(\mathbf{x},s)-\psi_n^*(\mathbf{x})\|_{C(\partial\Omega)}\right)\leq C^*h, \tag{4.6}$$

Also,

$$q_n^*(\mathbf{x})=\psi_n^*(\mathbf{x}),\mathbf{x}\in\partial\Omega. \tag{4.7}$$

Hence, because of (4.4), it is reasonable to assume that

$$\|q_n^*\|_{C^{2+\alpha}\left(\overline{\Omega}\right)}\leq C^*\ . \tag{4.8}$$

It follows from (4.2) that the following analogue of equation (3.10) holds

$$\begin{aligned}&\Delta q_n^*+A_{2,n}\left(h\sum_{j=0}^{n-1}\nabla q_j^*-\nabla T^*\right)\nabla q_n^* &(4.9)\\ =\ &A_{3,n}h\sum_{j=1}^{n-1}\Delta q_j^*+A_{4,n}\left(h\sum_{j=0}^{n-1}\nabla q_j^*-\nabla T^*\right)^2-A_{3,n}\Delta T^*+F_n^*(\mathbf{x}),\end{aligned}$$

where the error function $F_n^*(\mathbf{x})\in C^\alpha\left(\overline{\Omega}\right)$. This error function includes the error due to (4.6) as well the term $A_{1,n}\left(\nabla q_n^*\right)^2$. By (3.12) and (4.4) $|A_{1,n}|\left(\nabla q_n^*\right)^2(\mathbf{x})\leq 2\left(C^*\right)^2\bar{s}^2h,\mathbf{x}\in\Omega$. Let $\bar{s}>1$. By (4.5) we can re-denote $C^*:=2\left(C^*\right)^2\bar{s}^2$. Hence, (4.6) implies that it is reasonable to assume that

$$\|F_n^*(\mathbf{x})\|_{L_2(\Omega)}\leq C^*h. \tag{4.10}$$

It is convenient now to denote $\varphi(\mathbf{x},s) := \varphi(\mathbf{x},\mathbf{x}_0)$, where $\varphi(\mathbf{x},\mathbf{x}_0)$ is the function in (2.4). Since the function $\varphi(\mathbf{x},s)$ models the measured data, we assume that it is given with an error. This naturally produces an error in the function $\psi(\mathbf{x},s)$ in (3.7). An additional error is introduced in the averaging of functions $\psi(\mathbf{x},s), \psi^*(\mathbf{x},s)$ over the interval $[s_n, s_{n-1}]$. Let $\sigma > 0$ be a small parameter characterizing the level of the error in the data $\psi(\mathbf{x},s)$. Hence, it is reasonable to assume that

$$\|\psi_n^*(\mathbf{x}) - \psi_n(\mathbf{x})\|_{C(\partial\Omega)} \leq C^*(\sigma + h), \tag{4.11}$$

Remark 4.1. It should be noted that our experimental data $\varphi(\mathbf{x},s)$ are naturally given with a random noise and this function should be differentiated with respect to s, see (3.7). Although the differentiation of the noisy data is an ill-posed problem, there exist effective numerical regularization methods of its solution. However, since we work only with three values of the parameter s in our experimental data (because of some limitations of our device), we simply calculate the s derivative via the finite difference (subsection 7.2), and this does not lead to a degradation of our reconstruction results.

4.3 Our approximate mathematical model

In this model we basically assume that the upper bound for the tail function can become sufficiently small independently on $\overline{s}$. In addition, since we calculate the tail function $T(\mathbf{x},\overline{s})$ separately from the function q, we assume that the function $T(\mathbf{x},\overline{s})$ is given (but not the exact tail function $T^*(\mathbf{x},\overline{s})$). Although the smallness of T is supported by (3.4), the independence of that upper bound of this function from $\overline{s}$ does not follow from (3.4). Still this is one of two assumptions of our *approximate* mathematical model.

Analogously, although the Huygens-Fresnel theory of optics is not supported by the Maxwell's system (see section 8.1 of the classical textbook [11]), the "diffraction part" of the entire modern optical industry is based on the Huygens-Fresnel optics. More precisely, our approximate mathematical model $\overline{M}$ consists of the following two

Assumptions:

1. We assume that the number $\overline{s} > 1$ is sufficiently large and fixed. Also, the tail function $T(\mathbf{x},\overline{s})$ is given and tail functions $T^*(\mathbf{x},\overline{s}), T(\mathbf{x},\overline{s})$ have the forms

$$T^*(\mathbf{x},\overline{s}) = \frac{\ln w_0(\overline{s})}{\overline{s}^2} + r^*(\mathbf{x},\overline{s}),\ \mathbf{x}\in\Omega,\ r^* \in C^2\left(\overline{\Omega}\right), \tag{4.12}$$

$$T(\mathbf{x},\overline{s}) = \frac{\ln w_0(\overline{s})}{\overline{s}^2} + r(\mathbf{x},\overline{s}),\ \mathbf{x}\in\Omega,\ r \in C^2\left(\overline{\Omega}\right), \tag{4.13}$$

$$\|r^*\|_{C^2(\overline{\Omega})} \leq \frac{\xi}{2},\ \|r\|_{C^2(\overline{\Omega})} \leq \frac{\xi}{2}, \tag{4.14}$$

where $\xi \in (0,1)$ is a small parameter. Furthermore, the parameter ξ is independent on $\overline{s}$.

2. As the unknown vector $x \in B$ in Definition 4.1, we choose the vector function $\overline{q}(\mathbf{x}) = (q_1, ..., q_N)(x)$ in (3.15). In this case we will have only one iteration in Definition 4.1, i.e. $K = \overline{K} = 1$ in (4.1). We assume that there exists a number $c^* \in (0, C^*)$ independent on

the step size h of the partition of the interval $(\underline{s}, \overline{s})$ such that $\|\nabla q_n^*\|_{L_2(\Omega)} \geq c^*, n \in [1, N]$, and the number c^* is given.

Below we verify this approximate mathematical model $\overline{M}$ on experimental data. It is for the sake of our convergence analysis that we choose here the vector function $\overline{q}(\mathbf{x})$ rather than the coefficient $a(\mathbf{x})$ as our unknown function. This is because of some analytical difficulties associated with the presentation (3.16), (3.17). Indeed, below we will actually find finite dimensional approximations for components of the vector function $\overline{q}(\mathbf{x})$. Since in the most popular case of standard piecewise linear triangular finite elements such an approximation is a linear combination of those elements, then it will not belong to $H^2(\Omega)$ as required by (3.16), (3.17). On the other hand, finding $a(\mathbf{x})$ in the weak form of (5.1), (5.2) would require some interpolation estimates of the differences between functions q_n^* and their interpolations via the finite dimensional subspace G_m in the next subsection. The latter has its own "underwater rock" in terms of the convergence analysis.

By Definition 4.1 we need to prove uniqueness of the function $q^*(\mathbf{x}, s)$.

Lemma 4.1. *Assume that the tail function $T^*(\mathbf{x}, \overline{s})$ satisfying (4.12), (4.14) is given. Then there exists a small number $\mu = \mu(C^*, \Omega, \overline{s})$ depending on listed parameters such that if $(\overline{s} - \underline{s}) \in (0, \mu)$ and $\xi \in (0, \mu)$, then for $(\mathbf{x}, s) \in \Omega \times (\underline{s}, \overline{s})$ there exists at most one function $q^*(\mathbf{x}, s)$ satisfying conditions (4.2)-(4.5).*

Proof. Suppose that there exist two functions q_1^*, q_2^*. Let $\widetilde{q}^* = q_1^* - q_2^*$. By (4.3) $q_1^*, q_2^*, \widetilde{q}^* \in C^{2+\alpha}\left(\overline{\Omega}\right) \times C^1[\underline{s}, \overline{s}]$ and by (4.2)

$$\begin{gathered} \Delta\widetilde{q}^* - \frac{2}{s}\int\limits_s^{\overline{s}} \Delta\widetilde{q}^*(\mathbf{x}, \tau)\, d\tau - 2s^2 \nabla\widetilde{q}^* \int\limits_s^{\overline{s}} \nabla q_1^*(\mathbf{x}, \tau)\, d\tau - 2s^2 \nabla q_2^* \int\limits_s^{\overline{s}} \nabla\widetilde{q}^*(\mathbf{x}, \tau)\, d\tau \\ -4s \int\limits_s^{\overline{s}} \nabla\widetilde{q}^*(\mathbf{x}, \tau)\, d\tau \left(-\int\limits_s^{\overline{s}} (\nabla q_1^* + \nabla q_2^*)(\mathbf{x}, \tau)\, d\tau + \nabla T^* \right) + 2s^2 \nabla\widetilde{q}^* \nabla T^* = 0, \\ \widetilde{q}^*(\mathbf{x}, s) = 0, \forall (\mathbf{x}, s) \in \partial\Omega \times [\underline{s}, \overline{s}]. \end{gathered} \tag{4.15}$$

In particular, $\widetilde{q}^* \in H_0^1(\Omega), \forall s \in [\underline{s}, \overline{s}]$. Multiply both parts of equation (4.19) by $\widetilde{q}^*$ and integrate over $\Omega \times (\underline{s}, \overline{s})$. Then with a constant $B = B(C^*, \Omega, \overline{s}) > 0$ we obtain after standard calculations

$$\int\limits_{\underline{s}}^{\overline{s}} \|\widetilde{q}^*(\mathbf{x}, s)\|_{H^1(\Omega)}^2\, ds \leq B\mu \int\limits_{\underline{s}}^{\overline{s}} \|\widetilde{q}^*(\mathbf{x}, s)\|_{H^1(\Omega)}^2\, ds. \ \square$$

4.4 The finite dimensional approximation

Since we are concerned with the discrete version of the approximate global convergence theorem, we introduce a finite dimensional subspace $G_m \subset H_0^1(\Omega)$ with $\dim G_m = m$. A realistic example of the latter is the subspace, generated by triangular finite elements, which are piecewise linear functions. And we indeed work with these elements when solving above boundary value problems for functions q_n (the end of subsection 3.3). We assume that $f_x, f_z \in L_\infty(\Omega), \forall f \in G_m$. Since all norms in the subspace G_m are equivalent, then there

exists a constant $C_m = C_m(G_m)$ such that

$$\|\nabla f\|_{L_\infty(\Omega)} \leq C_m \|\nabla f\|_{L_2(\Omega)}, \ \forall f \in G_m, \ C_m \geq 2. \tag{4.16}$$

Here and below $\|\nabla f\|_{L_\infty(\Omega)} := \left(\|f_x\|^2_{L_\infty(\Omega)} + \|f_y\|^2_{L_\infty(\Omega)}\right)^{1/2}$ and the same for the $L_2(\Omega)$ norm. Since we want to approximate functions $p_n = q_n - \Psi_n$ (subsection 3.3) on the subspace G_m of the space $H^1_0(\Omega)$, rather than on the entire space $H^1_0(\Omega)$, then, in principle, we would need to introduce the error function in the weak solution identity (3.22). However, this would only complicate the proof of Theorem 4.1, while still leaving the idea of the proof the same. Hence, we assume below that

$$p_n, \eta \in G_m \text{ in (3.22)}, \ n \in [1, N]. \tag{4.17}$$

Consider a function $\Psi^*_n \in C^2\left(\overline{\Omega}\right)$ such that

$$\Psi^*_n \mid_{\partial\Omega} = \psi^*_n. \tag{4.18}$$

An example of this function is $\Psi^*_n(\mathbf{x}) = \chi(\mathbf{x}) q^*_n(\mathbf{x})$, where the function $\chi \in C^\infty\left(\overline{\Omega}\right), \chi(\mathbf{x}) = 1$ in a small neighborhood of $\partial\Omega$ and $\chi(\mathbf{x}) = 0$ outside of this neighborhood. The existence of such functions χ is known from the Real Analysis course. It follows from (4.8) and (4.11) that it is reasonable to assume that

$$\|\Psi_n - \Psi^*_n\|_{H^1(\Omega)} \leq C^*(\sigma + h). \tag{4.19}$$

Similarly with (3.20) let

$$f^*_n(\mathbf{x}) = A_{4,n}\left(h\sum_{j=0}^{n-1} \nabla q^*_j - \nabla T^*\right)^2 - A_{3,n}\Delta T^*. \tag{4.20}$$

Denote $p^*_n = q^*_n - \Psi^*_n$. Then, using (4.9) and (4.17), we obtain similarly with (3.22)

$$\begin{aligned} &\int_\Omega \nabla p^*_n \nabla\eta d\mathbf{x} - A_{2,n}\int_\Omega \left(h\sum_{j=0}^{n-1}\nabla q^*_j - \nabla T^*\right)\nabla p^*_n \eta d\mathbf{x} \\ = \ &-\int_\Omega \left\{\nabla\Psi^*_n\nabla\eta + \left[A_{2,n}\left(h\sum_{j=0}^{n-1}\nabla q^*_j - \nabla T^*\right)\nabla\Psi^*_n + f^*_n\right]\eta\right\} d\mathbf{x} \\ &+A_{3,n}h\int_\Omega \sum_{j=1}^{n-1}\nabla q^*_j\nabla\eta d\mathbf{x} - \int_\Omega F^*_n\eta d\mathbf{x}, \ \forall\eta \in G_m. \end{aligned} \tag{4.21}$$

We have

$$p^*_n = \overline{p}^*_n + \widehat{p}^*_n, \ q^*_n = (\overline{p}^*_n + \Psi^*_n) + \widehat{p}^*_n := \overline{q}^*_n + \widehat{p}^*_n, \ n \in [1, N], \tag{4.22}$$

where functions $\overline{p}_n^* \in G_m$ and functions $\widehat{p}_n^*$ belong to the orthogonal complement of the subspace G_m in the space $H_0^1(\Omega)$. Hence, $q_n^* - \overline{q}_n^* = \widehat{p}_n^*$. We assume that functions p_n^* are approximated so well by functions $\overline{p}_n^* \in G_m$ that

$$\|q_n^* - \overline{q}_n^*\|_{H^1(\Omega)} = \|\widehat{p}_n^*\|_{H^1(\Omega)} \leq \rho,\ n \in [1, N], \tag{4.23}$$

where $\rho \in (0,1)$ is a sufficiently small number whose specification follows from Theorem 4.1. Note that since the number C^* in (4.4), (4.5), (4.8) is assumed to be known, then, given a specific type of finite elements and the number ρ, it is usually possible to choose such a subspace G_m of those finite elements, which would guarantee the estimate (4.23). To do so, one should use standard interpolation estimates.

Substituting (4.22) in (4.21) and moving all terms with functions $\widehat{p}_j^*$ in the error function $F_n^*(\mathbf{x})$, we obtain an obvious analog of the integral identity (4.21). However, unlike (4.21), only functions $\overline{q}_j^*$ and $\overline{p}_n^*$ are involved in the left hand side of this identity. Since we do not want to change notations (for brevity), we denote $p_n^* := \overline{p}_n^*, q_n^* := \overline{q}_n^*$ and recall that $q_0^* = 0$. Hence, in these new notations we have similarly with (4.17)

$$p_n^* = q_n^* - \Psi_n^* \in G_m, n = 1, ..., N \text{ in (4.21)}. \tag{4.24}$$

Likewise, similarly with (4.8), it is natural to assume that in these new notations

$$\|\nabla q_n^*\|_{L_\infty(\Omega)} \leq C^*,\ \ \|p_n^* - \Psi_n^*\|_{L_\infty(\Omega)} \leq 2C^*. \tag{4.25}$$

To emphasize the dependence of the error function from the subspace G_m as well as from the number ρ in (4.23), we replace (4.10) with the following inequality

$$\left\|F_{n,m}^*(\mathbf{x})\right\|_{L_2(\Omega)} \leq C^*(\rho + h + \sigma). \tag{4.26}$$

4.5 Approximate global convergence theorem

Let $\xi, \rho, h, \sigma \in (0,1)$ be parameters introduced above. Denote $\gamma = \xi + \rho + h + \sigma$. The parameter γ characterizes several errors: the error in the data, the error in our approximations as well as the magnitude of the $C^2\left(\overline{\Omega}\right)$ norm of the tail (see (4.12)-(4.14) for the latter). The underlying reason of imposing the smallness assumption on the length of the interval $(\underline{s}, \overline{s})$ in Theorem 4.1 is that equations (3.21) for functions p_n are actually generated by the nonlinear equation (3.5) containing Volterra integrals. It is well known from the standard ODE course that these equations can be investigated only on a sufficiently small interval.

The approximate global convergence property in terms of Definition 4.1 and the approximate mathematical model of subsection 4.3 is proved in Theorem 4.1.

Theorem 4.1. *Let $\Omega \subset \mathbb{R}^2$ be a convex bounded domain with the boundary $\partial\Omega \in C^3$. Let $A(\Omega)$ be the area of the domain Ω. Asssume that $A(\Omega) \geq 1$ and denote $C_1 = C_1(\Omega) = C_0(\Omega)\sqrt{A(\Omega)} \geq 1$, where $C_0(\Omega) \geq 1$ is the constant in (3.19). Let $\overline{s} \geq 1$. Assume that the function $q^*(\mathbf{x}, s)$ satisfying (4.2), (4.3) exists and also that conditions (3.14), (4.4)-(4.8), (4.17)-(4.19), (4.21)-(4.26) and Assumptions 1,2 hold. Denote $M = 90\overline{s}^2 C_0 C^*, \beta = \overline{s} - \underline{s}$.*

Let $C_m \geq 1$ be the constant in (4.16). Assume that $\beta, \xi \in (0, \mu)$, where the parameter μ was introduced in Lemma 4.1. In addition, let

$$\beta \leq \frac{1}{M + C^*} = \frac{1}{90\overline{s}^2 C_1 C^* + C^*}, \tag{4.27}$$

$$\gamma \leq \frac{1}{90\overline{s}^2 C_1 C_m}. \tag{4.28}$$

Then for each $n \in [1, N]$ there exists unique solution p_n of the problem (3.22) satisfying (4.17). Let $q_n = p_n + \Psi_n$. Then the following estimates hold

$$\|\nabla q_n - \nabla q_n^*\|_{L_2(\Omega)} \leq (M + C^*)\,\gamma,\ \forall n \in [1, N] \tag{4.29}$$

$$\|\nabla q_n\|_{L_\infty(\Omega)} \leq 2C^*,\ \forall n \in [1, N]. \tag{4.30}$$

In addition, let in (4.23) the number $\rho \in (0, c^*/2)$ and

$$\gamma < \frac{1}{M}\left(\frac{c^*}{2} - \rho\right), \gamma < \frac{c^*}{2MN}, \tag{4.31}$$

where $c^* > 0$ is the constant of Assumption 2. Then (4.29) implies that

$$\frac{\|\nabla \overline{q} - \nabla \overline{q}^*\|_{L_2(\Omega)}}{\|\nabla \overline{q}\|_{L_2(\Omega)}} \leq \frac{2MN}{c^*}\gamma := \theta,\ \theta \in (0, 1), \tag{4.32}$$

where $\overline{q}^*(\mathbf{x}) = (q_1^*, ..., q_N^*)(x)$.

Remarks 4.2.

1. Estimate (4.32) means the approximate global convergence of the level θ (Definition 4.1) within the framework of our approximate mathematical model of subsection 4.3.

2. Although the number M depends on C_1, C^*, it is convenient to incorporate C^* in M in (4.27) and (4.29). Indeed, it follows from (4.43) that otherwise we would need to assume that M depends from the number N of functions q_n. On the other hand, since $Nh = \beta$ and h is a part of the parameter γ, then the dependence of M from N would cause additional difficulties in the proof below.

Proof. In this proof we use estimates (3.13) for numbers $A_{2,n}, A_{3,n}, A_{4,n}$ without further mentioning. Also, we use in this proof without further mentioning the following inequalities

$$\|v\|_{L_2(\Omega)} \leq \sqrt{A(\Omega)}\,\|v\|_{L_\infty(\Omega)} \leq C_1 \|v\|_{L_\infty(\Omega)},\ \forall v \in L_\infty(\Omega).$$

Since $\beta, \xi \in (0, \mu)$, then Lemma 4.1 implies that the function q^* is unique. Denote

$$\widetilde{q}_n(\mathbf{x}) = q_n(\mathbf{x}) - q_n^*(\mathbf{x}),\ \widetilde{p}_n(\mathbf{x}) = p_n(\mathbf{x}) - p_n^*(\mathbf{x}),\ \widetilde{f}_n(\mathbf{x}) = f_n(\mathbf{x}) - f_n^*(\mathbf{x}),$$
$$\widetilde{T}(\mathbf{x}) = T(\mathbf{x}) - T^*(\mathbf{x}),\ \widetilde{\Psi}_n(\mathbf{x}) = \Psi_n(\mathbf{x}) - \Psi_n^*(\mathbf{x}).$$

Since $q_0 = 0$, then estimates (4.29), (4.30) and (4.32) are valid for $n = 0$. Let $n \in [1, N]$. Assume that these estimates are valid for functions $q_j, j \in [0, n-1]$ and prove them for $j = n$.

For all numbers $a_1, a_2, b_1, b_2 \in \mathbb{R}$ we have $a_1b_1 - a_2b_2 = a_1\widetilde{b} + \widetilde{a}b_2$, where $\widetilde{a} = a_1 - a_2, \widetilde{b} = b_1 - b_2$. Subtract (4.21) from (3.22) and set in the resulting equality $\eta := \widetilde{p}_n$. Then

$$\|\nabla \widetilde{p}_n\|^2_{L_2(\Omega)} - A_{2,n} \int\limits_\Omega \left(h \sum_{j=0}^{n-1} \nabla q_j - \nabla T \right) \nabla \widetilde{p}_n \widetilde{p}_n d\mathbf{x}$$

$$= A_{2,n} \int\limits_\Omega \left(h \sum_{j=0}^{n-1} \nabla \widetilde{q}_j - \nabla \widetilde{T} \right) \nabla \left(p_n^* - \Psi_n^* \right) \widetilde{p}_n d\mathbf{x} \tag{4.33}$$

$$+ \int\limits_\Omega -\nabla \widetilde{\Psi}_n \nabla \widetilde{p}_n d\mathbf{x} - A_{2,n} \int\limits_\Omega \left(h \sum_{j=0}^{n-1} \nabla q_j - \nabla T \right) \nabla \widetilde{\Psi}_n \widetilde{p}_n d\mathbf{x}$$

$$- \int\limits_\Omega \widetilde{f}_n \widetilde{p}_n d\mathbf{x} + A_{3,n} \int\limits_\Omega h \sum_{j=0}^{n-1} \nabla \widetilde{q}_j \nabla \widetilde{p}_n d\mathbf{x} + \int\limits_\Omega F^*_{n,m} \widetilde{p}_n d\mathbf{x}.$$

Let lhs be the left hand side of (4.35). We now estimate lhs from the below using (3.13), (3.19), (4.14) as well as estimates (4.29) and (4.30) for functions $q_j, j \in [0, n-1]$. We have

$$lhs \geq \|\nabla \widetilde{p}_n\|^2_{L_2(\Omega)} - 8\overline{s}^2 C_1 \left(2\beta C^* + \gamma \right) \|\nabla \widetilde{p}_n\|^2_{L_2(\Omega)}. \tag{4.34}$$

Since $C_m \geq 2$, then by (4.27) and (4.28)

$$8\overline{s}^2 C_1 \left(2\beta C^* + \gamma \right) = \left(16\overline{s}^2 C_1 C^* \beta + 8\overline{s}^2 C_1 \right) < \frac{1}{3}.$$

Hence, (4.34) implies that

$$lhs \geq \frac{2}{3} \|\nabla \widetilde{p}_n\|^2_{L_2(\Omega)}. \tag{4.35}$$

We now estimate term-by-term the right hand side rhs of (4.33) from the above. We now estimate term-by-term the right hand side of (4.35) from the above. Without further mentioning, we use below in this proof (3.13), (3.19), (4.14), (4.19), (4.25)-(4.28), as well as estimates (4.29) and (4.30) for functions $q_j, j \in [0, n-1]$. In addition, we Cauchy-Schwarz inequality "with ε", which is $ab \geq -\varepsilon a^2/2 - b^2/(2\varepsilon), \forall a, b \in \mathbb{R}, \forall \varepsilon > 0$.

First,

$$A_{2,n} \left| \int\limits_\Omega \left(h \sum_{j=0}^{n-1} \nabla \widetilde{q}_j - \nabla \widetilde{T} \right) \nabla \left(p_n^* - \Psi_n^* \right) \widetilde{p}_n d\mathbf{x} \right|$$

$$\leq 16\overline{s}^2 C^* \left\| h \sum_{j=0}^{n-1} \nabla \widetilde{q}_j - \nabla \widetilde{T} \right\|_{L_2(\Omega)} \|\widetilde{p}_n\|_{L_2(\Omega)}$$

$$\leq 16\overline{s}^2 C^* \left(\beta \left(M + C^* \right) + 1 \right) \gamma C_1 \|\nabla \widetilde{p}_n\|_{L_2(\Omega)} \leq 32\overline{s}^2 C^* \gamma C_1 \|\nabla \widetilde{p}_n\|_{L_2(\Omega)}$$

$$\leq \frac{16}{\varepsilon}\overline{s}^4 \left(C^*\right)^2 + 16\varepsilon \left(C_1\right)^2 \left\|\nabla \widetilde{p}_n\right\|^2_{L_2(\Omega)}.$$

Thus,

$$A_{2,n}\left|\int\limits_\Omega \left(h\sum_{j=0}^{n-1}\nabla \widetilde{q}_j - \nabla \widetilde{T}\right)\nabla\left(p_n^* - \Psi_n^*\right)\widetilde{p}_n d\mathbf{x}\right| \leq \frac{16}{\varepsilon}\overline{s}^4 \left(C^*\right)^2 + 16\varepsilon \left(C_1\right)^2 \left\|\nabla \widetilde{p}_n\right\|^2_{L_2(\Omega)}. \quad (4.36)$$

We now estimate from the above the third line of (4.33),

$$\left|\int\limits_\Omega \nabla\widetilde{\Psi}_n \nabla \widetilde{p}_n d\mathbf{x} + A_{2,n}\int\limits_\Omega \left(h\sum_{j=0}^{n-1}\nabla q_j - \nabla T\right)\nabla\widetilde{\Psi}_n \widetilde{p}_n d\mathbf{x}\right|$$

$$\leq \left\|\nabla\widetilde{\Psi}_n\right\|_{L_2(\Omega)}\left\|\nabla\widetilde{p}_n\right\|_{L_2(\Omega)} + 8\overline{s}^2\left(2C^*\beta+\gamma\right)C_1\left\|\nabla\widetilde{\Psi}_n\right\|_{L_2(\Omega)}\left\|\nabla\widetilde{p}_n\right\|_{L_2(\Omega)}$$

$$\leq \left[C^* + 16\overline{s}^2 C^*\beta + 8\overline{s}^2\gamma\right]\gamma C_1\left\|\nabla\widetilde{p}_n\right\|_{L_2(\Omega)}.$$

Since by (4.5) $C^* \geq 1$, then (4.27) and (4.28) imply $\left[C^* + 16\overline{s}^2 C^*\beta + 8\overline{s}^2\gamma\right] \leq 2C^*$. Thus,

$$\left|\int\limits_\Omega \nabla\widetilde{\Psi}_n \nabla \widetilde{p}_n d\mathbf{x} + A_{2,n}\int\limits_\Omega \left(h\sum_{j=0}^{n-1}\nabla q_j - \nabla T\right)\nabla\widetilde{\Psi}_n \widetilde{p}_n d\mathbf{x}\right| \quad (4.37)$$

$$\leq \frac{2}{\varepsilon}\left(C^*\right)^2\gamma^2 + \frac{\varepsilon}{2}\left(C_1\right)^2\left\|\nabla\widetilde{p}_n\right\|^2_{L_2(\Omega)}.$$

Next, using (3.20) and (4.20), we similarly obtain

$$\left|\int\limits_\Omega \widetilde{f}_n\widetilde{p}_n d\mathbf{x}\right| \leq \frac{2}{\varepsilon}\gamma^2 + \frac{\varepsilon}{2}C_1^2\left\|\nabla\widetilde{p}_n\right\|^2_{L_2(\Omega)}. \quad (4.38)$$

Next,

$$A_{3,n}\left|\int\limits_\Omega h\sum_{j=0}^{n-1}\nabla\widetilde{q}_j\nabla\widetilde{p}_n d\mathbf{x}\right| \leq 8\overline{s}^2\left\|h\sum_{j=0}^{n-1}\nabla\widetilde{q}_j\right\|_{L_2(\Omega)}\left\|\nabla\widetilde{p}_n\right\|_{L_2(\Omega)}$$

$$\leq 8\overline{s}^2\beta\left(M+C^*\right)\gamma\left\|\nabla\widetilde{p}_n\right\|_{L_2(\Omega)} \leq \frac{4}{\varepsilon}\overline{s}^4\gamma^2 + \frac{\varepsilon}{2}\left\|\nabla\widetilde{p}_n\right\|^2_{L_2(\Omega)}.$$

Thus,

$$A_{3,n}\left|\int\limits_\Omega h\sum_{j=0}^{n-1}\nabla\widetilde{q}_j\nabla\widetilde{p}_n d\mathbf{x}\right| \leq \frac{4}{\varepsilon}\overline{s}^4\gamma^2 + \frac{\varepsilon}{2}\left\|\nabla\widetilde{p}_n\right\|^2_{L_2(\Omega)}. \quad (4.39)$$

Finally

$$\left| \int_\Omega F^*_{n,m} \widetilde{p}_n d\mathbf{x} \right| \leq \frac{(C^*)^2}{2\varepsilon}\gamma^2 + \frac{\varepsilon}{2} C_1^2 \varepsilon \left\| \nabla \widetilde{p}_n \right\|^2_{L_2(\Omega)}. \tag{4.40}$$

Let rhs be the right hand side of (4.33). Summing up estimates (4.36)-(4.40) and keeping in mind that $\overline{s}, C_1, C^* \geq 1$, we obtain

$$rhs \leq \frac{24\overline{s}^4 (C^*)^2}{\varepsilon}\gamma^2 + 20 C_1^2 \varepsilon \left\| \nabla \widetilde{p}_n \right\|^2_{L_2(\Omega)}. \tag{4.41}$$

Choose $\varepsilon = (60C_1^2)^{-1}$. Substituting this in (4.41) and then comparing with (4.35), we obtain

$$\left\| \nabla \widetilde{p}_n \right\|_{L_2(\Omega)} \leq 66\overline{s}^2 C_1 C^* \gamma < M\gamma. \tag{4.42}$$

Thus, (4.42) and Lax-Milgram theorem imply that there exists unique weak solution $\widetilde{p}_n \in G_m$ of the problem (3.22) satisfying (4.17). Since $\widetilde{q}_n = \widetilde{p}_n + \widetilde{\Psi}_n$, then (4.19) and (4.42) imply that

$$\left\| \nabla \widetilde{q}_n \right\|_{L_2(\Omega)} \leq M\gamma + C^*\gamma = (M + C^*)\gamma. \tag{4.43}$$

The latter establishes (4.27). Next, by (4.16) and (4.28) $\left\| \nabla \widetilde{q}_n \right\|_{L_\infty(\Omega)} \leq MC_m\gamma \leq C^*$. Hence,

$$\left\| \nabla q_n \right\|_{L_\infty(\Omega)} = \left\| \nabla q_n^* + \nabla \widetilde{q}_n \right\|_{L_\infty(\Omega)} \leq 2C^*,$$

which establishes (4.28). Recall now that our functions q_n^*, which were used in this proof above, are actually functions $\overline{q}_n^*$, which were introduced in (4.22), and the error estimate (4.23) holds. Hence, using (4.29) and the first inequality (4.31), we obtain

$$\begin{aligned} \left\| \nabla q_n \right\|_{L_2(\Omega)} &= \left\| (\nabla q_n - \nabla \overline{q}_n^*) + (\nabla \overline{q}_n^* - \nabla q_n^*) + \nabla q_n^* \right\|_{L_2(\Omega)} \\ &\geq \left\| \nabla q_n^* \right\|_{L_2(\Omega)} - \left\| \nabla q_n - \nabla \overline{q}_n^* \right\|_{L_2(\Omega)} - \left\| \nabla \overline{q}_n^* - \nabla q_n^* \right\|_{L_2(\Omega)} \\ &\geq c^* - M\gamma - \rho \geq \frac{c^*}{2}. \end{aligned}$$

Thus, $\left\| \nabla q_n \right\|_{L_2(\Omega)} \geq c^*/2$. Next, using the latter inequality (4.29) and (4.31), we obtain

$$\frac{\left\| \nabla \overline{q} - \nabla \overline{q}^* \right\|_{L_2(\Omega)}}{\left\| \nabla \overline{q} \right\|_{L_2(\Omega)}} \leq \frac{N \max_n \left\| \nabla q_n - \nabla q_n^* \right\|_{L_2(\Omega)}}{\min_n \left\| \nabla q_n \right\|_{L_2(\Omega)}} \leq \frac{2MN}{c^*}\gamma, \tag{4.44}$$

$$\frac{2MN}{c^*}\gamma \quad := \theta \in (0,1). \tag{4.45}$$

Estimates (4.44) and (4.45) imply (4.32). $\square$

5 Numerical Implementation

Since this implementation was described in detail in [18], we outline it only briefly here for the convenience of the reader. As to the functions q_n, we have sequentially calculated them via the FEM solving Dirichlet boundary value problems (3.9), (3.10) with the assumption (3.14). As it was mentioned in the end of subsection 3.3, we have used standard triangular finite elements. Two important questions which are discussed in this section are about approximating the function $a(\mathbf{x})$ and the tail function $T(\mathbf{x})$.

5.1 Approximation of the function $a(\mathbf{x})$

We reconstruct the target coefficient $a(\mathbf{x})$ via backwards calculations as follows. First, we reconstruct the function $\widetilde{w}(x, s_N)$ by (3.16). In principle we can reconstruct the target coefficient $a(\mathbf{x})$ from (3.17). However, because our finite elements to calculate functions q_j in (3.16) are piecewise linear ones, it is numerically unstable to calculate second derivatives in (3.17). Hence, we first reconstruct an approximation for the function $u(\mathbf{x}, s_N)$ as $u(\mathbf{x}, s_N) = \exp[\widetilde{w}(\mathbf{x}, s_N)]$. Next, since in (2.1) the source $\mathbf{x}_0 \notin \overline{\Omega}$, we use equation (2.1) in the weak form as

$$-\int\limits_{\Omega} \nabla u \nabla \eta_p d\mathbf{x} = \int\limits_{\Omega} a u \eta_p d\mathbf{x}, \tag{5.1}$$

where the test function $\eta_p(\mathbf{x}), p \in [1, P]$ is a quadratic finite element of a computational mesh with the boundary condition $\eta_p(\mathbf{x})|_{\partial\Omega} = 0$. The number P is finite and depends on the mesh we choose. Equalities (5.1) lead to a linear algebraic system which we solve. Since this formulation is complex but standard, it is omitted here. Interested readers can see [13]. Finally, we let

$$a(\mathbf{x}) = \max\left(\overline{a}(\mathbf{x}), k^2\right). \tag{5.2}$$

5.2 Construction of the tail function

The above construction of functions q_n depends on the tail function T. In this subsection we state briefly our heuristic procedure of approximating the tail function, see [18,22,23] for details. This procedure consists of two stages. First, we find a first guess for the tail using the asymptotic behavior of the solution of the problem (2.1), (2.2) as $|\mathbf{x}_0| \to \infty$ (Lemma 2.2), as well as boundary measurements. On the second stage we refine the tail.

We display in Fig. 1 the boundary data collection scheme in our experiment. We have used six locations of the light sources, see Fig. 1a. Sources number 1,2 and 3 are the ones which model the source $\mathbf{x}_0$ running along the straight line L, see (2.4). The distance between these sources was six (6) millimeters. Each light source means drilling a small hole in the phantom to fix the source position. It was impossible to place more sources in a phantom of this size that mimics actual mouse head. So, since the data for the functions q_n are obtained via the differentiation with respect to the source position, we have used only two functions q_1, q_2. Fortunately, it was sufficient for our goal of imaging of abnormalities to use only

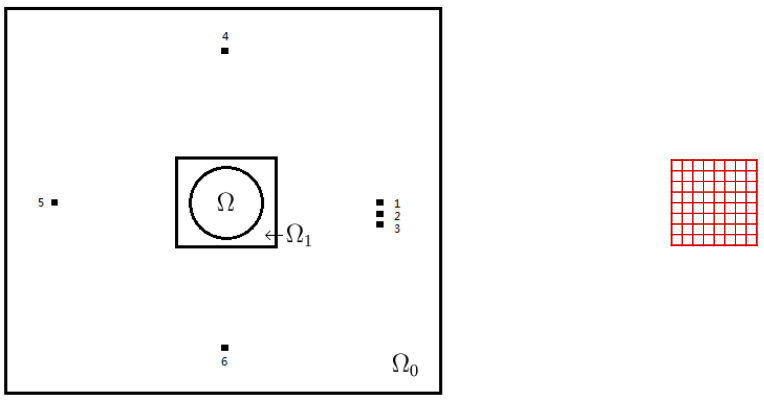

(a) (b)

Figure 1: *The schematic diagrams of inverse problem domain and light source locations. (a) Illustrates a layout of the inverse problem setting in 2-D. The circular disk* Ω *corresponds to a horizontal cross-section of the hemisphere part of phantom (the supposed "mouse head" in animal experiments), The computational domain* Ω_1 *is a rectangle containing* Ω *inside, 6 light sources are located outside of the computational domain. Because of limitations of our device, we use only three locations of the light source along one line (number 1,2,3) to model the source* $\mathbf{x}_0$ *running along the straight line* L*. Light sources numbered 1,4,5,and 6 are used to construct an approximation for the tail function. (b) Depicts the computational domain* $\Omega_1 = \{(x,z), |x| < 5.83, |z| < 5.83\}$ *(unit:mm) and its rectangular meshes for tail functions and inverse calculations for Globally Convergent method in this paper. Actual mesh is much dense than these displayed. The diagram is not scaled to actual sizes*

two functions q_1, q_2. Sources 1,4,5,6 (Fig. 1a) were used to approximate the tail function as described below. We construct that approximation in the domain Ω_1 depicted on Fig. 1b. This domain is (units in millimeters)

$$\Omega_1 := \{\mathbf{x} = (x,z) : x_1 = -5.83 < x < x_2 = 5.83, z_1 = -5.83 < z < z_2 = 5.83\}. \tag{5.3}$$

5.2.1 The first stage of approximating the tail

Since this stage essentially relies on positions of sources 1,4,5,6, it makes sense to describe this stage in detail here, although it was also described in [18]. The light sources are placed as far as possible from the domain Ω_1, so that the asymptotic approximations of solutions are applicable. Denote the position of the light source number j as $\mathbf{s}^{(j)}$. First, consider the light source number 1. Denote

$$S^{(1)} := S^{(1)}\left(x, z, \mathbf{s}^{(1)}\right) = \left|(x,z) - \mathbf{s}^{(1)}\right|. \tag{5.4}$$

Using (2.5), Theorem 2.1 and Lemma 2.2, we obtain for the function $\widetilde{w} = \ln u$

$$\widetilde{w}\left(x,z,\mathbf{s}^{(1)}\right) = -kS^{(1)} - \ln\left(2\sqrt{2\pi}\right) - \frac{1}{2}\ln S^{(1)} + p_\infty(x,z) + O\left(\frac{1}{S^{(1)}}\right), S^{(1)} \to \infty. \quad (5.5)$$

Since by (5.3) $\widetilde{w}\left(x,z_1,\mathbf{s}^{(1)}\right) = \varphi\left(\mathbf{x},\mathbf{s}^{(1)}\right), \mathbf{x} \in \partial\Omega \cap \{z = z_1\}$, we use (5.5) to approximate the unknown function $p_\infty(x,z_1)$ as

$$p_\infty(x,z_1) = \widetilde{w}\left(x,z_1,\mathbf{s}^{(1)}\right) + kS\left(x,z_1,\mathbf{s}^{(1)}\right) + \frac{1}{2}\ln\left(\frac{\pi}{2S\left(x,z_1,\mathbf{s}^{(1)}\right)}\right). \quad (5.6)$$

Formula (5.6) gives the value of $p_\infty(x,z_1)$ only at $z = z_1$. Since Ω_1 is a square, we set the first guess for the tail as the one which is obtained from (5.6) by simply extending the values at $z = z_1$ to the entire domain of Ω_1,

$$\widetilde{w}\left(x,z,\mathbf{s}^{(1)}\right) = -kS^{(1)}\left(x,z,\mathbf{s}^{(1)}\right) - \ln\left(2\sqrt{2\pi}\right) - \frac{1}{2}\ln S^{(1)}\left(x,z,\mathbf{s}^{(1)}\right) + p_\infty(x,z_1),$$

where the function $S\left(x,z,\mathbf{s}^{(1)}\right)$ is given in (5.4). Next, we compute the function $u\left(x,z,\mathbf{s}^{(1)}\right) = \exp\left(\widetilde{w}\left(x,z,\mathbf{s}^{(1)}\right)\right)$ and get $a^{(1)}(x,z), (x,z) \in \Omega$ via (5.1), (5.2).

For light sources 4, 5 and 6, we repeat the above procedure to get $a^{(4)}(x,z), a^{(5)}(x,z)$ and $a^{(6)}(x,z)$ respectively. Then we consider the average coefficient

$$\overline{a}(x,z) = \frac{1}{4}\left(a^{(1)}(x,z) + a^{(4)}(x,z) + a^{(5)}(x,z) + a^{(6)}(x,z)\right) \quad (5.7)$$

and set

$$a(x,z) := \max\left(\overline{a}(x,z), k^2\right). \quad (5.8)$$

Next, we solve the forward problem (2.1), (2.2) for the light $\mathbf{s}^{(3)}$ with this coefficient $a(x,z)$ again to get $u(x,z,\overline{s}), \overline{s} = \left|\mathbf{s}^{(3)}\right|$. The final approximate tail function obtained on the first stage is

$$T_1(x,z) = \frac{\ln u(x,z,\overline{s})}{\overline{s}^2}. \quad (5.9)$$

5.2.2 The second stage for the tail

The second stage involves an iterative process that enhances the first approximation for the tail (5.9). We describe this stage only brief here referring to [18] for details. In this case we use only one source Number 3, $\mathbf{s}^{(3)}$. Recall that $\left|\mathbf{s}^{(3)}\right| = \overline{s}$. Denote $a_1(\mathbf{x}) := a(x,z)$, where the function $a(x,z)$ is one calculated in (5.7), (5.8). Next, we solve the following boundary value problem

$$\begin{aligned} \Delta u_1 - a_1(\mathbf{x})\, u_1 &= 0, \mathbf{x} \in \Omega_1, \\ u_1|_{\partial\Omega_1} &= \varphi(\mathbf{x},\overline{s}), \mathbf{x} \in \partial\Omega_1. \end{aligned}$$

Then, we iteratively solve the following boundary value problems

$$\begin{aligned} \Delta w_m - a_m(\mathbf{x})\, w_m &= [a_m(\mathbf{x}) - a_{m-1}(\mathbf{x})]\, u_{m-1},\ m \geq 2, \\ w_m|_{\partial\Omega_1} &= 0. \end{aligned}$$

We set $u_m := u_{m-1} + w_m$. Next, using (5.1) and (5.2) with $u := u_m$, we find the function $a_{m+1}(\mathbf{x})$. We have computationally observed that this iterative process provides a convergent sequence $\{a_m(\mathbf{x})\}$ in $L_2(\Omega_1)$. We stop iterations at $m := m_1$, where m_1 is defined via

$$\frac{\|a_{m_1} - a_{m_1-1}\|_{L_2(\Omega_1)}}{\|a_{m_1-1}\|_{L_2(\Omega_1)}} \leq \varepsilon, \tag{5.10}$$

where $\varepsilon > 0$ is a small number of our choice, and the norm in $L_2(\Omega_1)$ is understood in the discrete sense. Next, assuming that $u_{m_1} > 0$, we set for the tail

$$T(\mathbf{x}) = \frac{1}{\overline{s}^2} \ln u_{m_1}(\mathbf{x}). \tag{5.11}$$

Then we proceed with calculating of functions q_n as described above.

Remarks 5.1.

1. Even though we can reconstruct an approximation for the function $a(\mathbf{x})$ from the tail function (5.11) without computing functions q_n, we have found in our previous numerical experiments with computationally simulated data that finding functions q_n significantly improves the image accuracy.

2. Unfortunately we cannot yet prove that functions $a_m(\mathbf{x}) \to a(\mathbf{x})$. Likewise, we cannot yet prove analytically the positivity of functions u_m. Also, we cannot prove analytically that functions u_m converge, nor that our tail T (5.11) is close to the correct tail T^*. Nevertheless, we have consistently observed this closedness in our previous publications [18,22,23]. For example, it can be seen from Figure 2 of [23] that our constructed tail function is quite close to the real one. Also, by (5.11) $T(\mathbf{x}) := T(\mathbf{x},\overline{s}) = O(1/\overline{s}^2)$, which is similar with (3.4), (4.12)-(4.14).

6 Experimental Data

We now describe our experimental setup for collecting the optical tomography data from an optical phantom. This phantom is a man-made subject that has the same optical property as animals. Such a phantom is a well-accepted standard to test reconstruction methods for real applications before animal experiments.

Fig. 2 is a photograph of our measurement setup. The center of the picture is the phantom (rectangular box with a hemisphere on top surface) which, in particular, contains a hidden inclusion inside (not visible in this photo). The hemisphere mimics the mouse head in animal experiments of stroke studies, and a hidden inclusion mimics a blood clot. The four needles are laser fibers that provide light sources in our experiments. The fiber on the right

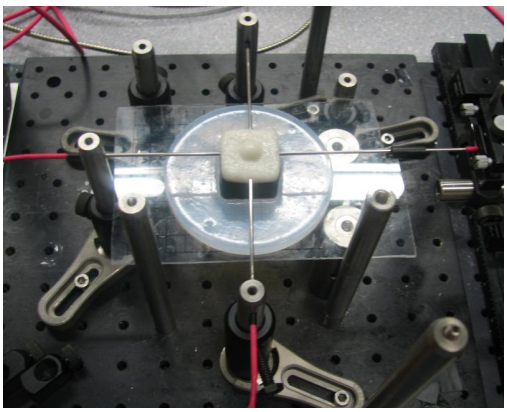

Figure 2: *Photograph of the experimental setup, an optical phantom is connected by 4 laser fibers, one on the righthand side is movable to locations 1,2, and 3. The gelatin made phantom is of a shape of rectangular box with a hemisphere on top surface, mimic a mouse head with a mask exposing crown part of the mouse. A CCD camera mounted above phantom (not shown), takes light intensity measurements of the top surface of phantom.*

hand side of Fig. 2 can be moved to three other positions which are source positions 1,2,3 on Fig. 1a. Three other fibers represent positions 4,5,6 of the source on Fig. 1a. A CCD camera is mounted directly above the setup (not shown in photo), and the camera focus on the top surface of the phantom. CCD stands for Charge Coupled Device. CCD camera with its sensitivity and response range is commonly used for near infrared laser imaging of animals.

The purpose of this experimental setup is to study the feasibility of using our numerical method in stroke model of animal study. In the case of a real animal the top hemisphere (meshed shape in Fig. 3a) is to be replaced by a mouse head and the rectangular block of phantom to be replaced by an optical mask filled with a "matching" fluid (a liquid with same optical as mouse skin/skull). The image reconstruction should provide the spatial distribution of the optical coefficient $a(\mathbf{x})$ (directly related to blood content) in a 2-D cross-section of the animal brain.

We have modified specific geometrical parameters to match actual experiments. In addition, while in our above algorithm is for the 2-D case, experimental data are obviously in 3-D. Hence, we collect the data at the boundary of a 2-D cross-section. And in our computations we ignore the dependence on the variable which is orthogonal to this cross-section. The latter is similar with the case of a quite successful treatment of the experimental data of Electrical Impedance Tomography by a non-locally convergent algorithm in [17].

Specifically, our inverse reconstruction is performed in a 2-D plane depicted in Fig. 3b, with the optical parameter distribution of the medium inside the circle (at the center of Fig. 3b) as an unknown coefficient in the photon diffusion model. Should we need a diagnosis of a different cross-section of mouse brain in animal experiments, we need a different optical mask filled with matching fluid, and repeat both the experiment and the reconstruction.

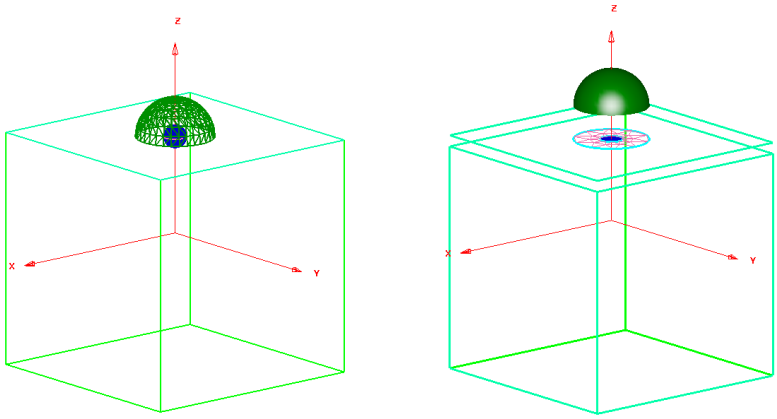

(a) (b)

Figure 3: *The schematic diagrams of our data acquisition process. (a) Schematically depicts a 3-D phantom and its hidden inclusion (shown in meshed surface) 5mm below the phantom. The light source is placed at various locations on the top surface of the rectangular block (shown in Fig. 1a) and light intensity measurements are taken on the top surface of phantom. (b) Shows the measurement surface by a CCD camera. The data are collected from the surface of the hemisphere as well as un-shaded area of top rectangle, both area are lifted from the phantom in this drawing for a better illustrative purpose. The rectangular figure in Fig. 3b also illustrates in the middle a 2-D cross-section (meshed circle) of the presumed "animal head", at the boundary of which light intensity data are collected for reconstruction. The light intensity at the 2-D cross-section (except for the boundary) is obstructed by the top surface of the hemisphere. Light sources are also located in the same plane as this cross-section area. The 2-D inverse problem is solved in this cross-section via ignoring the dependence on the orthogonal coordinate.*

The geometry of the phantom (shown in a vertical central cross-section) is depicted in Fig. 4 with dimensions specified. The phantom is shaped by a hemisphere (diameter 13 mm) on top of a cube of 30mm × 30mm × 30mm. A spherical hollow of 5 mm diameter is inside the phantom, with its top 5mm below the top surface (Fig. 4). The location of this hollow is symmetric here but can be in any place when needed. The hollow is our inclusion which we fill with different kinds of liquid from ink/intralipid mix to model strokes by blood clots. Intralipid is a product for fat emulsion, mimic the response of human or animal tissue to light at wavelengths in the red and infrared ranges. The phantom is made of gelatin mixed with the intralipid. The percentage of intralipid content is adjustable. So that the phantom has the same optical parameters as the background medium of the target animal model. At the location of the inclusion (the hollow), we inject ink/intralipid mixed fluids which has optical absorption rate 2 times, 3 times, 4 times of the background. Also, we use the pure black ink to test our reconstruction method for the case of infinite absorption. Different levels of the absorption ratio are used to validate our method for its ability for different blood clots. Light

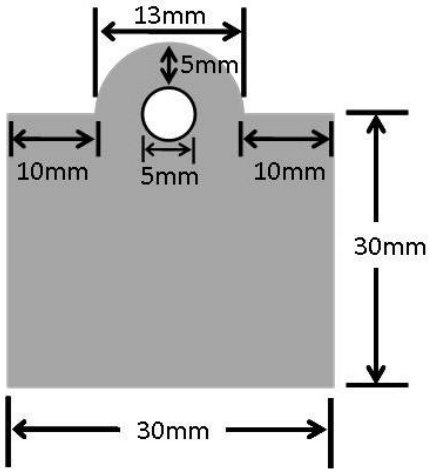

Figure 4: *Dimensions of the phantom, shown in a vertical cross-section at center of the phantom from side view. The circle in Fig. 1a corresponds to the blue circle in Fig. 3b. This is also corresponds to the boundary of the 13mm diameter circle at a top view above the rectangular box (but not related to circle or semicircle in this graph). The 5mm diameter hollow sphere is for placement of inclusions, filled with liquids of different compositions to emulate strokes. The hidden inclusion is 5mm below the top surface.*

intensity measurements are taken from direct above the semicircle in Fig. 4. We note that Fig. 1a shows a top view of the layout but Fig. 4 shows a cross-section from side view. The disk region Ω in Fig. 1a corresponds to the meshed area in Fig. 3b as well as a horizontal cross-section of 13mm hemisphere. The reason we use such a geometry is that we need to test our capability to reconstruct inclusions at several different depth (moving up and down vertically as in Fig. 4) as well as different locations (moving horizontally in Fig. 3b).

7 Processing Experimental Data

As it is always the case when working with imaging from experimental data, we need to make several steps of data pre-processing before applying our inverse algorithm.

7.1 Computational domains

In particular, we use several computational domains. The computational domains and meshes used in our numerical calculation involve four domains. Fig. 5a - Fig. 5c and Fig. 1b are the finite element meshes on each of these domains $\Omega, \Omega_0, \Omega_0 \setminus \Omega, \Omega_1$ respectively. In actual computations we use more refined meshes for each domain than those illustrated. So, figures are not scaled to actual sizes.

Here the disk Ω is the domain of interest that contains the inclusion, corresponding to

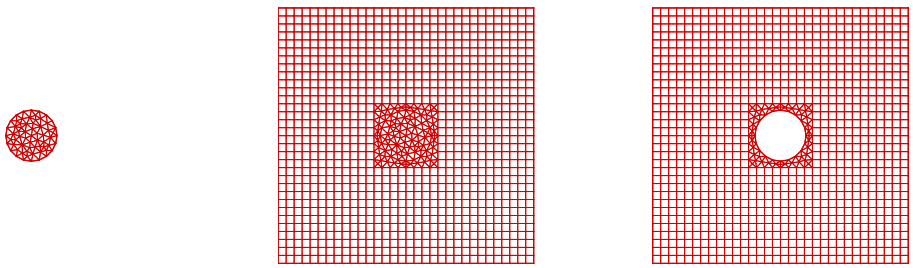

(a) Ω (b) Ω_0 (c) $\Omega_0 \backslash \Omega$

Figure 5: *(a) Shows* $\Omega = \{(x,z), \sqrt{x^2+z^2} < 4.63\}$ *(unit:mm) with a triangular mesh, the domain representing a cross-section of our phantom, and the inclusion inside* Ω *is to be reconstructed. (b) Shows* $\Omega_0 = \{(x,z), |x| < 23.32, |z| < 23.32\}(unit : mm)$*, the domain contains* Ω *and light sources for forward problem calculation. Meshed small square is the domain* Ω_1 *which is the same as on Fig. 1b. Computations of the inverse problem are performed in* Ω_1*. (c) Shows* $\Omega_0 \backslash \Omega$ *the domain used for data processing. To smooth out the measurement noise, equation (2.1) with the Dirichlet boundary conditions* $u\mid_{\partial\Omega} = \varphi(x, x_0)$*,* $u\mid_{\partial\Omega_0} = 0$ *is solved in* $\Omega_0 \backslash \Omega$*. Then the smoothed data along* $\partial\Omega_1$ *is used for inverse problem.*

the meshed area in Fig. 3b. It reflects a cross-section of the hemisphere of phantom in Fig. 3b. The light intensity data used in our computation originates from measurements at $\partial\Omega$ by taking pictures with CCD camera on the top of phantom as discussed, shown in Fig. 3b. The CCD camera collected data is acquired for the entire top surface exposed, and we extract only the needed data for $\partial\Omega$ i.e., the circle in Fig. 3b by getting data at these locations, as boundary values. There $\Omega = \left\{(x,z) \,|\sqrt{x^2+z^2} \leq 4.63mm\right\}$.

On Fig. 5 Ω_0 is a large domain, which can be interpreted as a truncated plane $\mathbb{R}^2$. Indeed, one cannot practically solve the forward problem (2.1), (2.2) in the infinite space $\mathbb{R}^2$. Light sources are located in $\Omega_0 \backslash \Omega$. The background simulation and calibration of background parameters are performed in Ω_0. To smooth the noise data, equation (2.1) is solved in $\Omega_0 \backslash \Omega$ for each source position, which is similar with [22]. Because of (2.3), we use $a(\mathbf{x}) := k^2$ for $x \in \Omega_0 \backslash \Omega$. In this procedure the Dirichlet boundary condition at $\partial\Omega$ is taken from experimental data, and we use the zero Dirichlet boundary condition at $\partial\Omega_0$. As a result, we obtain the smoothed Dirichlet boundary condition at $\partial\Omega_1$ for each source location. The boundary condition corresponding the source number are used to construct the tail function in Ω_1. Also, we solve the inverse problem in Ω_1 and $\Omega \subset \Omega_1$.

7.2 Data pre-processing and approximations of boundary conditions

As it was stated in subsection 7.1, to smooth out our measurement data, we solve the Dirichlet boundary problem for equation (2.1) with $a(\mathbf{x}) \equiv k^2$ for $\mathbf{x} \in \Omega_0 \setminus \Omega$ (Fig. 5c). Namely,

$$\begin{aligned} \Delta u - k^2 u &= -\delta\left(\mathbf{x}-\mathbf{s}^{(i)}\right), \mathbf{x} \in \Omega_0 \setminus \Omega, \\ u\mid_{\partial\Omega} &= \varphi\left(\mathbf{x}, \mathbf{s}^{(i)}\right),\ u\mid_{\partial\Omega_0} = 0. \end{aligned} \tag{7.1}$$

Here $k^2 = 3\mu_s'\mu_a$ is the background value and $\varphi\left(\mathbf{x},\mathbf{s}^{(i)}\right)$ is the experimentally measured data for the light source $\mathbf{s}^{(i)}$. Let $\overline{\varphi}\left(\mathbf{x}, \mathbf{s}^{(i)}\right)$ be the trace of the solution of the Dirichlet boundary value problem (7.1) at $\mathbf{x} \in \partial\Omega_1$. We solve the inverse problem in the square Ω_1 with the smoothed data $u\mid_{\partial\Omega_1} = \overline{\varphi}\left(\mathbf{x}, \mathbf{s}^{(i)}\right)$. We have shown in [23, 25] that solving inverse problems in the original domain Ω and extended domain Ω_1 are equivalent mathematically. But numerically the noisy component in $\overline{\varphi}\left(\mathbf{x}, \mathbf{s}^{(i)}\right)$ is much smaller than in $\varphi\left(\mathbf{x}, \mathbf{s}^{(i)}\right)$. This smoothing effect takes place because of the well known smoothing property of solutions of elliptic equations, see Theorem 6.17 in [16].

As it was mentioned in subsection 5.2, because of limitations of our device, we can use only three source positions on the line L, which are source positions number 1,2,3 on Fig. 1a. Thus, we work only with functions q_1, q_2. To calculate Dirichlet boundary conditions $\psi_i(\mathbf{x}), x \in \partial\Omega_1, i = 1, 2$ for functions q_1, q_2, we use (3.7) and proceed as follows

$$\psi_i(\mathbf{x}) = \frac{1}{s_i^2}\left(\frac{\ln\overline{\varphi}\left(\mathbf{x}, \mathbf{s}^{(i+1)}\right) - \ln\overline{\varphi}\left(\mathbf{x}, \mathbf{s}^{(i)}\right)}{s_{i+1} - s_i}\right) - \frac{2\ln\overline{\varphi}\left(\mathbf{x}, \mathbf{s}^{(i)}\right)}{s_i^3}, s_i = \left|\mathbf{s}^{(i)}\right|, i = 1, 2; \overline{s} = \left|\mathbf{s}^{(3)}\right|.$$

7.3 The forward problem and calibration

We now address the question on which value of k^2 one should use when working with experimental data. The optical properties of the phantom background (without the hidden inclusion) is known theoretically from the concentration of intralipid in the mix. However, there is a discrepancy between the theoretical value and actual measurement. Before we solve the inverse problem to image hidden inclusions, we calibrate our model by adjusting the background value of k^2 to experimental data measured for the reference medium, which is the phantom without inclusion, i.e. the hollow space is filled with same intralipid solution as that in the phantom itself.

First, we numerically solve the forward problem with the source position $\mathbf{s}^{(1)}$ in the domain Ω_0 without any inclusion,

$$\begin{aligned} \Delta u - k^2 u &= -A\delta\left(\mathbf{x}-\mathbf{s}^{(1)}\right), \mathbf{x} \in \Omega_0, \\ u\mid_{\partial\Omega_0} &= 0, \end{aligned} \tag{7.2}$$

where $k^2 = 3\mu_s'\mu_a$ is the background value. Then we calibrate the parameter μ_a (fixing μ_s') as well as the amplitude $A > 0$ of light source in our model (7.2) to match the measured

light intensity for $\mathbf{s}^{(1)}$ for the uniform background. We do not know the number A. Thus, we choose A in such a way that $u_{comp}\left(\mathbf{x}_{\max}, \mathbf{s}^{(1)}\right) \approx u_{meas}\left(\mathbf{x}_{\max}, \mathbf{s}^{(1)}\right)$. Here $\mathbf{x}_{\max}$ is the brightest point, i.e. the far right point on $\partial\Omega$, being closest to the light source. Also, $u_{comp}\left(\mathbf{x}_{\max}, \mathbf{s}^{(1)}\right)$ and $u_{meas}\left(\mathbf{x}_{\max}, \mathbf{s}^{(1)}\right)$ are computed and measured light intensities respectively. Next, we should approximate the constant k^2. To do this, we take another sampling point $\mathbf{x}_{\min}$ with the minimum light intensity, which is the farthest left point on $\partial\Omega$. Next we consider ratios $R_{comp}\left(k^2\right), R_{meas}$, where

$$R_{comp}\left(k^2\right) = \frac{u_{comp}\left(\mathbf{x}_{\max}, \mathbf{s}^{(1)}\right)}{u_{comp}\left(\mathbf{x}_{\min}, \mathbf{s}^{(1)}\right)}, \; R_{meas} = \frac{u_{meas}\left(\mathbf{x}_{\max}, \mathbf{s}^{(1)}\right)}{u_{meas}\left(\mathbf{x}_{\min}, \mathbf{s}^{(1)}\right)}.$$

These ratios are independent on the number A in (7.2). We choose k^2 such that $R_{comp}\left(k^2\right) \approx R_{meas}$. As a result, the calibrated value of k^2 was $k^2 = 2.403$. This computed value matches quite well the theoretical value of 2.4 of the intralipid solution we have used.

8 Reconstruction Results

Let $a_{incl} = a\left(\mathbf{x}\right)$ be the value of $a\left(\mathbf{x}\right)$ inside the inclusion and $a_b = k^2 = 2.403$ be the value of the coefficient $a\left(\mathbf{x}\right)$ in the background, which was computed in subsection 7.3. Our ratios a_{incl}/a_b where

$$\frac{a_{incl}}{a_b} = 2, 3, 4, \infty. \tag{8.1}$$

These contrasts are created by injecting different liquids in the hollow. The value $a_{incl}/a_b = \infty$ means that the inclusion was filled with a black absorber, i.e. black ink.

As described in sub-subsection 5.2.1, we construct the "asymptotic tail" on the first stage using light sources 1,4,5, and 6. The image of the function $\overline{a}\left(x, z\right)$ in (5.7) is depicted on Fig. 6.

In all our examples $\varepsilon = 10^{-5}$ in (5.10). Fig. 7 depicts the resulting image from our experimental data for the contrast $a_{incl}/a_b = 3$. Reconstructed images for other contrasts $a_{incl}/a_b = 2, 4, \infty$ are similar, although maximal values of $a\left(\mathbf{x}\right)$ vary accordingly, which is natural. Recall that $a_b = k^2 = 2.403$. The finally reconstructed results for contrasts $a_b^{-1} \max a\left(\mathbf{x}\right)$ are listed in Table 1. Note that our above reconstruction algorithm does not use any knowledge of neither the location of the inclusion, nor the contrast value a_{incl}/a_b.

Table 1. Reconstructed values of the contrast $a_b^{-1} \max a\left(\mathbf{x}\right)$ within imaged inclusions and they relative errors, $a_b = 2.403$, compare with (8.1)

The true contrast a_{incl}/a_b	$a_b^{-1} \max a\left(\mathbf{x}\right)$	Relative Error
2	2.11	0.056
3	2.9	0.032
4	4.22	0.057
∞	6.69	unknown

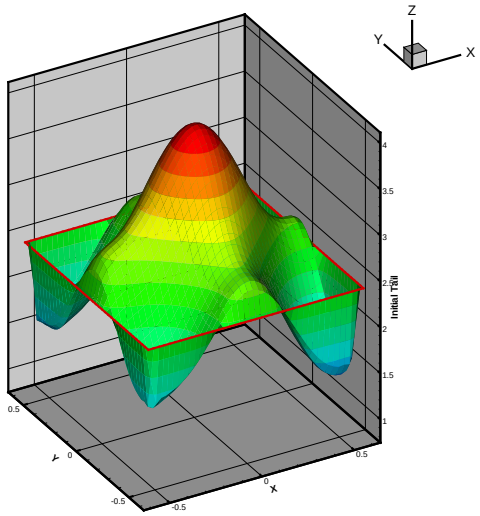

Figure 6: *The function $a(x,z)$ in (5.7) is depicted. This function was obtained on the first stage procedure for the tail (sub-subsection 5.2.1). The inclusion/background contrast (8.1) was $a_{incl}/a_b = 3$. Images for other values of this contrast listed in (8.1) were similar.*

9 Summary

Using experimental data, we have verified the approximately globally convergent numerical method of [18] for a Coefficient Inverse Problem for an elliptic equation. These data mimic imaging of a clot in the head of a mouse. We have introduced a new concept of the approximate global convergence property and have established this property for the discrete case of a finite number of finite elements, unlike the continuous case of [18]. Images of inclusions from experimental data are quite accurate, including both inclusion/background contrasts and locations of inclusions. Note that accurate values of contrasts are usually hard to reconstruct via locally convergent algorithms. On the other hand, these values are especially important for our target application, since they might be used for monitoring stroke treatments.

Acknowledgments

The work of all authors was supported by the National Institutes of Health grant number 1R21NS052850-01A1. In addition, the work of MVK was supported by the U.S. Army Research Laboratory and U.S. Army Research Office under the contract/grant number W911NF-08-1-0470.

References

[1] M. Abramowitz and A. Stegun, *Handbook of Mathematical Functions* (Washington, DC: National Bureau of Standards), 1964.

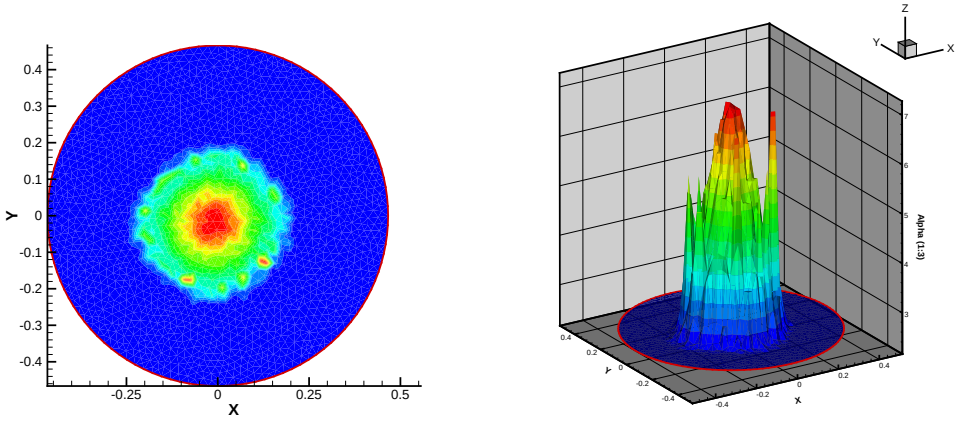

(a) (b)

Figure 7: *A sample of the image from experimental data. (a) The reconstructed function* $a(\mathbf{x})$ *for the case* $a_{incl}/a_b = 3$ *in (8.1) is displayed. (b) The 3-D view of (a). The vertical axis shows the reconstructed values of the function* $a(\mathbf{x})$*, see Table 1 for more details.*

[2] N.V. Alexeenko, V.A. Burov and O.D. Rumyantseva, Solution of a three-dimensional acoustical inverse scattering problem: II. Modified Novikov algorithm, *Acoust. Phys.*, 54, 407-419, 2008.

[3] R.R. Alfano, R.R. Pradhan and G.C. Tang, Optical spectroscopic diagnosis of cancer and normal breast tissues, *J. Opt. Soc. Am. B,* 6, 1015-1023, 1989.

[4] S. Arridge, Optical tomography in medical imaging, *Inverse Problems,* 15, 841-893, 1999.

[5] A.B. Bakushinsky, T. Khan and A. Smirnova, Inverse problem in optical tomography and its numerical investigation by iteratively regularized methods, *J. Inverse and Ill-Posed Problems,* 13, 537-551, 2005.

[6] H. Bateman and A. Erdelyi, *Tables of Integral Transforms*, V.1, New York, McGraw Hill, 1954.

[7] L. Beilina and M.V. Klibanov, A globally convergent numerical method for a coefficient inverse problem, *SIAM J. Sci. Comp.,* 30, 478-509, 2008.

[8] L. Beilina and M.V. Klibanov, Synthesis of global convergence and adaptivity for a hyperbolic coefficient inverse problem in 3D, *J. Inverse and Ill-posed Problems,* 18, 85-132, 2010.

[9] L. Beilina and M.V. Klibanov, *A posteriori* error estimates for the adaptivity technique for the Tikhonov functional and global convergence for a coefficient inverse problem, *Inverse Problems,* 26, 045012, 2010.

[10] L. Beilina and M.V. Klibanov, Reconstruction of dielectrics from experimental data via a hybrid globally convergent/adaptive inverse algorithm, *Inverse Problems,* 26, 125009, 2010.

[11] M. Born and E. Wolf, *Principles of Optics: Electromagnetic Theory of Propagation, Interference and Diffraction of Light*, Cambridge University Press, 1970.

[12] V.A. Burov, S.A. Morozov and O.D. Rumyantseva, Reconstruction of fine-scale structure of acoustical scatterers on large scale contrast background, *Acoust. Imaging,* 26, 231-238, 2002.

[13] P.G. Ciarlet, *The Finite Element Method for Elliptic Problems*, SIAM, Philadelphia , 2002.

[14] H.W. Engl, M. Hanke and A. Neubauer, *Regularization of Inverse Problems*, Kluwer Academic Publishers, Boston, 2000.

[15] A. Friedman, *Partial Differential Equations Of Parabolic Type*, Prentice Hall, Inc., Englewood Cliffs, N.J., 1964.

[16] D. Gilbarg and N.S. Trudinger, *Elliptic Partial Differential Equations Of the Second Order*, Springer-Verlag, New York, 1983.

[17] D. Isaacson, J.L. Mueller, J.C. Newell and S. Siltanen, Reconstructions of chest phantoms by the D-bar method for electrical impedance tomography, *IEEE Trans. Med. Imaging*, 23, 821-828, 2004.

[18] M.V. Klibanov, J. Su, N. Pantong, H. Shan and H. Liu, A globally convergent numerical method for an inverse elliptic problem of optical tomography, *Applicable Analysis*, 6, 861-891, 2010.

[19] M.V. Klibanov, M.A. Fiddy, L. Beilina, N. Pantong and J. Schenk, Picosecond scale experimental verification of a globally convergent numerical method for a coefficient inverse problem, *Inverse Problems*, 26, 045003, 2010.

[20] A.V. Kuzhuget, L.Beilina, M.V. Klibanov and V.G. Romanov, Approximate global convergence and quasi-reversibility for a coefficient inverse problem with backscattering data, submitted for publication, preprint is available on-line at http://www.ma.utexas.edu/mp_arc.

[21] J. Mueller and S. Siltaren, Direct reconstruction of conductivities from boundary measurements, *SIAM J. Sci. Comp.*, 24, 1232-1266, 2003.

[22] N. Pantong, J. Su, H. Shan, M.V. Klibanov and H. Liu, A globally accelerated reconstruction algorithm for diffusion tomography with continuous-wave source in arbitrary convex shape domain, *Journal of the Optical Society of America, A*, 26, 456-472 2009.

[23] H. Shan, M.V. Klibanov, J. Su, N. Pantong and H. Liu, A globally accelerated numerical method for optical tomography with continuous wave source, *J. Inverse and Ill-Posed Problems,* 16, 765-792, 2008.

[24] J. Su, H. Shan, H. Liu and M.V. Klibanov, Reconstruction method from a multiplesite continuous-wave source for three-dimensional optical tomography, *J. Optical Society of America A,* 23, 2388-2395, 2006.

[25] A.N. Tikhonov, A.V. Goncharsky, V.V. Stepanov and A.G. Yagola, *Numerical Methods for Solutions of Ill-Posed Problems,* Kluwer, London, 1995.